

Neural Projected Quantum Dynamics: a systematic study

Luca Gravina,^{1,2} Vincenzo Savona,^{1,2} and Filippo Vicentini^{3,4}

¹*Institute of Physics, Ecole Polytechnique Fédérale de Lausanne (EPFL), CH-1015 Lausanne, Switzerland*

²*Center for Quantum Science and Engineering, Ecole Polytechnique Fédérale de Lausanne (EPFL), CH-1015 Lausanne, Switzerland*

³*CPHT, CNRS, Ecole Polytechnique, Institut Polytechnique de Paris, 91120 Palaiseau, France.*

⁴*Collège de France, Université PSL, 11 place Marcelin Berthelot, 75005 Paris, France*

(Dated: December 11, 2024)

We address the challenge of simulating unitary quantum dynamics in large systems using Neural Quantum States, focusing on overcoming the computational instabilities and high cost of existing methods. This work offers a comprehensive formalization of the projected time-dependent Variational Monte Carlo (p-tVMC) method by thoroughly analyzing its two essential components: stochastic infidelity minimization and discretization of the unitary evolution. We investigate neural infidelity minimization using natural gradient descent strategies, identifying the most stable stochastic estimators and introducing adaptive regularization strategies that eliminate the need for manual adjustment of the hyperparameter along the dynamics. We formalize the specific requirements that p-tVMC imposes on discretization schemes for them to be efficient, and introduce four high-order integration schemes combining Taylor expansions, Padé approximants, and Trotter splitting to enhance accuracy and scalability. We benchmark our adaptive methods against a 2D Ising quench, matching state of the art techniques without manual tuning of hyperparameters. This work establishes p-tVMC as a highly promising framework for addressing complex quantum dynamics, offering a compelling alternative for researchers looking to push the boundaries of quantum simulations.

CONTENTS

I. Introduction	2	B. Control variates for the conditional Monte-Carlo estimator [Eq. (22)]	17
1. Neural Quantum Dynamics	2	C. Derivation of the gradient estimators	18
2. Projected Neural Quantum Dynamics and open challenges	2	1. Derivation of the ∇_{cmc} gradient estimator [Eq. (26)]	18
II. Integration schemes	3	2. Derivation of the $\nabla_{\text{cv-smc}}$ gradient estimator [Eq. (27)]	19
A. Generic formulation of p-tVMC schemes	3	3. Derivation of the ∇_{smc} gradient estimator [Eq. (25)]	20
B. Trotter decomposition	4	D. Covariance structure, Rao-Blackwellization, and variance reduction	21
C. Taylor decomposition	4	E. Lowering sampling cost by reweighting	22
D. Linear Product Expansion (LPE)	4	F. Machine precision on small systems and the limitation of Monte Carlo sampling	23
E. Padé Product Expansion (PPE)	4	G. Exact application of diagonal operators	23
F. Diagonally-exact split schemes	5	1. ZZ-operations	24
III. State compression Optimizations	6	H. Neural network architectures	25
A. The generic fidelity optimization problem	6	1. Convolutional neural networks	25
B. Natural Gradient Descent	6	2. Vision Transformer	25
C. Stochastic estimators	7	References	27
1. Fidelity	7		
2. Gradient	9		
3. Large number of parameters (NTK) limit	10		
4. Autonomous damping	10		
IV. Numerical Experiments	11		
A. Small-scale experiments	12		
B. Large-scale experiments	13		
V. Conclusions and outlooks	14		
A. Details on LPE and PPE schemes	15		
1. Linear Product Expansion (LPE)	15		
2. Padé Product Expansion (PPE)	16		
a. Unitarity of Padé Product Expansions	17		

I. INTRODUCTION

Simulating the dynamics of a quantum system is essential for addressing various problems in material science, quantum chemistry, quantum optimal control, and for answering fundamental questions in quantum information [1–3]. However, the exponential growth of the Hilbert space makes this one of the most significant challenges in computational quantum physics, with only few tools available to simulate the dynamics of large, complex systems without introducing systematic biases or relying on uncontrolled approximations.

To manage the exponential growth of the Hilbert space, quantum states can be encoded using efficient compression schemes [4]. While tensor network methods [5–10], particularly Matrix Product States [11–15], excel in simulating large one-dimensional models with short-range interactions, extending them to higher dimensions is problematic. Such extensions, either rely on uncontrolled approximations [16, 17], or incur in an exponential costs when encoding area-law entangled states [18], making them poorly suited for investigating strongly correlated, higher-dimensional systems or unstructured lattices, such as those encountered in chemistry or quantum algorithms [19–23].

Recently, Neural Quantum States (NQS) have garnered increasing attention as a non-linear variational encoding of the wave-function capable, in principle, of describing arbitrarily entangled states, both pure [24–28] and mixed [29–33]. This approach compresses the exponentially large wave-function into a polynomial set of parameters, with no restrictions on the geometry of the underlying system. The added flexibility, however, comes at a cost: unlike matrix product states whose bond dimension can be adaptively tuned via deterministic algorithms, neural network optimizations are inherently stochastic, making it hard to establish precise error bounds.

Despite the limitations of neural networks not being fully understood [34, 35], recent studies have demonstrated that NQS can be reliably optimized to represent the ground state of computationally challenging, non-stoquastic, fermionic, or frustrated Hamiltonians, arising across various domains of quantum physics [36–45]. However, for the more complex task of simulating quantum dynamics, NQS have yet to show significant advantages over existing methods.

1. Neural Quantum Dynamics

There are two families of variational algorithms for approximating the direct integration of the Schrödinger equation using variational ansätze: time-dependent Variational Monte Carlo (tVMC) [46] and projected tVMC (p-tVMC), formalized in Ref. [47]. The former, tVMC, linearizes both the unitary evolution and the variational ansatz, casting the Schrödinger equation into an explicit

algebraic-differential equation for the variational parameters [46, 48]. The latter, p-tVMC, relies on an implicit optimization problem to compute the parameters of the wave function at each timestep, using low-order truncations of the unitary evolution such as Taylor or Trotter expansions.

Of the two methods, tVMC is regarded as the least computationally expensive, as it avoids the need to solve a nonlinear optimization problem at every step. It has been successfully applied to simulate sudden quenches in large spin [24, 49–51] and Rydberg [52] lattices, quantum dots [53] as well as finite temperature [54, 55] and out of equilibrium [33, 56, 57] systems. However, while stable for (log-)linear variational ansätze such as Jastrow [52] or Tensor Networks, the stiffness of the tVMC equation [58] appears to increase with the nonlinearity of the ansatz, making integration particularly hard for deep networks. Contributing to this stiffness is the presence of a systematic statistical bias in the evaluation of the dynamical equation itself, which would be exponentially costly to correct [47]. Although the effect of this noise can be partially regularised away [49], this regularization procedure introduces additional bias that is difficult to quantify. As of today, the numerous numerical issues inherent to tVMC make its practical application to non-trivial problems difficult, with the estimation of the actual error committed by the method being unreliable at best.

2. Projected Neural Quantum Dynamics and open challenges

The projected time-dependent Variational Monte Carlo method offers a viable, albeit more computationally intensive, alternative by decoupling the discretization of the physical dynamics from the nonlinear optimization of the variational ansatz, thereby simplifying the analysis of each component. So far, the discretization problem has been tackled using established schemes such as Runge-Kutta [59] or Trotter [47, 60–62]. These methods do not fully leverage the specific properties of VMC approaches and, as a result, the existing body of work [47, 59, 63] has been limited to second-order accuracy in time, struggling to provide general, scalable solutions. Similarly, the nonlinear optimization problem has mainly been addressed using first-order gradient descent techniques, neglecting the benefits offered by second-order optimization strategies.

In this manuscript, we investigate both aspects of p-tVMC — discretization and optimization — independently, addressing the shortcomings detailed above with the goal of enhancing accuracy, reducing computational costs, and improving stability and usability.

Specifically, in Section II we introduce a new family of discretization schemes tailored for p-tVMC, achieving higher accuracy for equivalent computational costs. In Section III we conduct an in-depth analysis of the nonlinear optimization problem of infidelity minimization,

identifying the most effective stochastic estimator and introducing a new adaptive optimization scheme that performs as well as manually tuned hyperparameters, eliminating the need for manual adjustment. Finally, in Section IV we benchmark several of our methods against a challenging computational problem: a quench across the critical point of the two-dimensional transverse field Ising model.

II. INTEGRATION SCHEMES

Consider the generic evolution equation

$$|\psi_{t+dt}\rangle = e^{\hat{\Lambda}dt} |\psi_t\rangle, \quad (1)$$

where $\hat{\Lambda} = -i\hat{H}$ for some K -local time-independent Hamiltonian \hat{H} with K increasing at most polynomially in the system size N . The fundamental challenge for the numerical integration of Eq. (1) lies in the dimensionality of the Hilbert space \mathcal{H} scaling exponentially with system size, that is, $\dim(\mathcal{H}) \sim \exp(N)$. This makes it impossible to merely store in memory the state-vector $|\psi\rangle$, let alone numerically evaluate or apply the propagator.

Variational methods address the first problem by encoding an approximate representation of the state at time t into the time-dependent parameters θ_t of a variational ansatz, while relying on Monte Carlo integration to compute expectation values [24, 64, 65]. Within this framework, the McLachlan variational principle is used to recast Eq. (1) as the optimization problem [4]

$$\theta_{t+dt} = \underset{\theta}{\operatorname{argmin}} \mathcal{L}\left(|\psi_\theta\rangle, e^{\hat{\Lambda}dt} |\psi_{\theta_t}\rangle\right), \quad (2)$$

where \mathcal{L} is a suitable loss function quantifying the discrepancy between two quantum states. Various choices for \mathcal{L} are possible, the one adopted throughout this work is presented and discussed in Section III.

tVMC and p-tVMC confront Eq. (2) differently. The former, tVMC, linearizes both the unitary evolver and the ansatz, reducing Eq. (2) to an explicit first-order nonlinear differential equation in the parameters [24, 48]. In contrast, p-tVMC, relies on higher-order discretizations of the unitary evolver to efficiently solve the optimization problem in Eq. (2) at each timestep.

In Section II A we present a general formulation of p-tVMC which allows us to identify a generic set of requirements that discretization schemes should satisfy. We revisit the established Trotter and Runge-Kutta methods from this perspective in Sections II B and II C. Sections II D to II F introduce a new family of discretization schemes tailored to the specific structure of p-tVMC, which reach higher order in dt with a lower computational complexity.

A. Generic formulation of p-tVMC schemes

In this section, we explore expansions of the infinitesimal time-independent propagator in Eq. (2) in the form of a product series

$$e^{\hat{\Lambda}dt} = \prod_{k=1}^s \hat{V}_k^{-1} \hat{U}_k + \mathcal{O}\left(dt^{o(s)+1}\right), \quad (3)$$

where the number of elements s in the series is related to the order of the expansion $o = o(s)$. This decomposition is chosen for the following reasons:

- There are no summations. Therefore, the terms $\hat{V}_k^{-1} \hat{U}_k$ in the series can be applied sequentially to a state, without the need to store intermediate states and recombine them.
- The single step of p-tVMC can efficiently embed an operator inverse at every sub-step.

By utilizing this discretization, the parameters after a single timestep dt are found by solving a sequence of s subsequent optimization problems, with the output of each substep serving as the input for the next. Specifically, setting $\theta_t \equiv \theta^{(0)}$, and $\theta_{t+dt} \equiv \theta^{(s)}$, we can decompose Eq. (2) as

$$\theta^{(k)} = \underset{\theta}{\operatorname{argmin}} \mathcal{L}\left(\hat{V}_k |\psi_\theta\rangle, \hat{U}_k |\psi_{\theta^{(k-1)}}\rangle\right), \quad (4)$$

with $0 < k < s$. This optimization does not directly compress the variational state $|\psi_\theta\rangle$ onto the target state $|\phi\rangle$. Instead, it matches two versions of these states transformed by the linear operators \hat{V}_k and \hat{U}_k . A careful tuning of \hat{V}_k and \hat{U}_k can be seen as a form of preconditioning, initializing the optimization closer to the solution and potentially accelerating convergence.

Equation (4) can be solved efficiently with variational Monte Carlo methods provided all operators $\{\hat{V}_k, \hat{U}_k\}$ are log-sparse (or K -local). In what follows we explore proficient choices for the set $\{\hat{V}_k, \hat{U}_k\}$. Two conditions guide our search for an optimal expansion scheme :

- Equation (3) should match Eq. (2) to a specified order in dt , denoted as o , ensuring accurate time evolution up to this order.
- The computational complexity of solving Eq. (4), which is proportional to sN_c with N_c the number of connected elements of $\{\hat{V}_k, \hat{U}_k\}$, must scale at most polynomially in the number of particles N and in the order o of the method.

Table I summarizes our analysis, including both established discretization schemes, and the four new ones introduced in this manuscript.

Name	Sec.	substeps	order	N_c	unitary
Trotter	II B	$\mathcal{O}(N)$	2	$\mathcal{O}(2)$	✓
Taylor	II C	1	o	$\mathcal{O}(N^o)$	✗
LPE- o	II D	o	o	$\mathcal{O}(N)$	✗
PPE- o	II E	$\frac{o}{2}$	o	$\mathcal{O}(2N)$	✓
S-LPE- o	II F	†	o	$\mathcal{O}(N)$	✗
S-PPE- o	II F	o -1†	o	$\mathcal{O}(2N)$	$o = 2$

TABLE I. Discretization schemes compatible with p-tVMC. We denote by s the number of substeps (optimizations), o the order of the integration scheme, and N_c the connected elements (complexity) of the operators entering the optimization problem. We remark that the PPE- o scheme has only even orders o and is the only scheme that is exactly unitary for any choice of the truncation order o . The S-PPE scheme is exactly unitary only for $o = 2$. †: We were not able to derive an analytic expression connecting the order of the diagonally-exact split schemes. Semi-analytically we could determine that for S-LPE- o the first few substeps and orders are $(s, o) = (1, 1), (2, 2), (4, 3)$ and for S-PPE- o they are $(s, o) = (1, 2), (2, 3), (3, 4)$.

B. Trotter decomposition

A prototypical product series decomposition of a unitary operator is the Suzuki–Trotter decomposition [66]. In this approach, $\hat{\Lambda}$ is expressed as a sum of local terms, and the exponential of the sum is approximated as a product of the exponentials of the individual terms. The decomposition of $\hat{\Lambda}$ is not unique and can be tailored to the specifics of the problem to maximize computational efficiency [67].

While Suzuki–Trotter decompositions can be extended to arbitrary order, in practice, their use in NQS is typically limited to second order in dt , as seen in Refs. [47] and [60]. The key advantage of this approach is that it approximates the operator’s action in a manner where state changes are highly localized, which simplifies the individual optimization problems in Eq. (4) and tends to improve their convergence.

However, despite these benefits, Suzuki–Trotter decompositions face two main limitations: the truncation to second order in dt and the scaling of the number of optimizations with the system size, both of which hinder computational efficiency in large-scale applications.

C. Taylor decomposition

Another relevant decomposition to consider is the order- s Taylor approximation of the propagator. Its expression

$$e^{\hat{\Lambda}dt} = \sum_{k=0}^s \frac{(\hat{\Lambda}dt)^k}{k!} + \mathcal{O}(dt^{s+1}), \quad (5)$$

can be viewed within the framework of Eq. (3) as a single optimization problem ($s = 1$) of the form in Eq. (4) with $\hat{V}_1 = \mathbb{1}$ and $\hat{U}_1 = \sum_{k=0}^s (\hat{\Lambda}dt)^k / k!$. This approach satisfies condition (i) by matching the desired order of accuracy in dt , but it fails to meet condition (ii) related to computational efficiency. Indeed, computing $\hat{U}_1 |\psi_\theta\rangle$ requires summing over all N_c connected elements of \hat{U}_1 . As the order o increases, higher powers of $\hat{\Lambda}$ introduce a growing number of such connected elements, with $N_c \sim \mathcal{O}(N^o)$. This approach incurs a computational cost that scales exponentially in o , making it unviable at higher orders. Furthermore, this approach cannot reasonably be used in continuous space simulations, where the square of the Laplacian cannot be efficiently estimated.

D. Linear Product Expansion (LPE)

We now introduce a new scheme circumventing the limitations of the previous approaches. We consider the linear operator $\hat{T}_a \equiv \mathbb{1} + a\hat{\Lambda}dt$ with $a \in \mathbb{C}$ and expand the unitary evolver as a series of products of such terms,

$$e^{\hat{\Lambda}dt} = \prod_{i=1}^s \hat{T}_{a_i} + \mathcal{O}(dt^{s+1}). \quad (6)$$

The expansion is accurate to order $o(s) = s$. The complex-valued coefficients a_i are determined semi-analytically by matching both sides of the equation above order by order up to $o(s)$. At second order, for example, we find $a_1 = (1 - i)/2$ and $a_2 = (1 + i)/2$. Further details on the scheme and on the computation of the coefficients are provided in Appendix A. Tabulated values for a_i can be found in Table IV.

We call this method LPE- o for *Linear product expansion*, where o is the order of the method, related to the number of sub-steps s by $o(s) = s$. Each substep corresponds to an optimization problem with $\hat{V}_k = \mathbb{1}$, and $\hat{U}_k = \hat{T}_{a_k}$. The advantage of LPE over Taylor schemes (Section II C) is that the former defines an s -substep scheme of order s with a step-complexity $\mathcal{O}(sN)$, linear in s . This greatly outperforms Runge-Kutta style expansions for this particular application, enabling scaling to arbitrary order in dt , simultaneously satisfying conditions (i) and (ii).

It was noted in Ref. [53] that the coefficients a_i of this expansion are the complex roots of the order s Taylor polynomial. While this is a handy trick to compute them numerically, this approach is not general enough to represent the multi-operator expansions that we will analyze below in Sections II E and II F.

E. Padé Product Expansion (PPE)

We now present schemes reaching order $2s$ with only s sub-steps of marginally-increased complexity. We con-

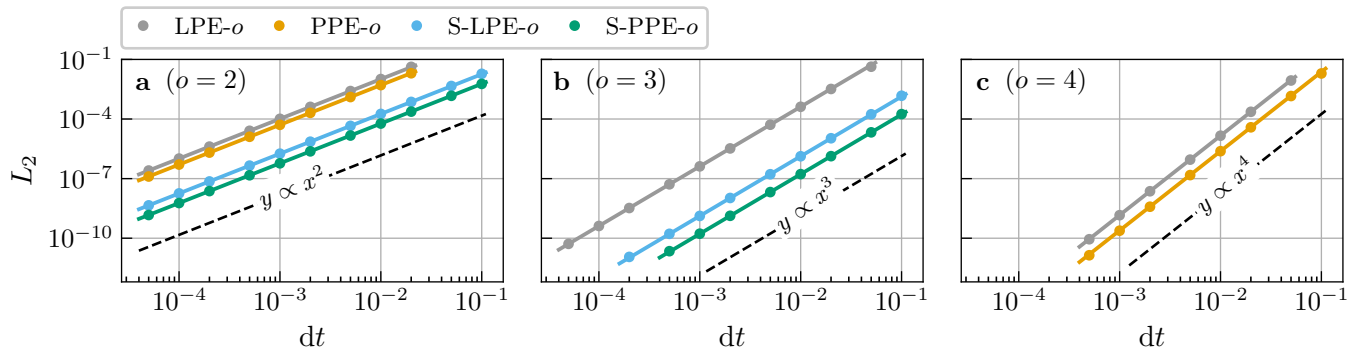


FIG. 1. Global truncation error accumulated at time $t = 1$ for LPE and PPE integrators, and their splitted counterparts, of orders $o = 2$ (a), $o = 3$ (b), and $o = 4$ (c). The evolution is carried out under the Hamiltonian in Eq. (32) simulating on a 4×4 lattice with the same quench dynamics investigated in Section IV B. The accumulated error for an integrator of order o scales as dt^o , with the local error scaling as dt^{o+1} . Both splitted and non-splitted integrators are shown, demonstrating the power of the splitting in reducing the prefactor of the error.

sider the operator $\hat{P}_{b,a} \equiv \hat{T}_b^{-1} \hat{T}_a$ and expand the evolver as a series of products of such terms,

$$e^{\hat{\Lambda} dt} = \prod_{i=1}^s \hat{P}_{b_i, a_i} + \mathcal{O}(dt^{2s+1}). \quad (7)$$

The expansion is accurate to order $o(s) = 2s$. We call this method PPE- s for *Padé product expansion*, because the single term $\hat{P}_{b,a}$ corresponds to a (1,1) Padé approximation [68]. The scheme is explicitly constructed to take advantage of the structure of the optimization problems in Eq. (4), exploiting the presence of a matrix inverse in the expansion (3). While atypical for standard ODE integrators, as it would introduce an unjustified overhead, in our case this simply translates into optimizations where $\hat{V}_i = \hat{T}_{b_i}$, and $\hat{U}_i = \hat{T}_{a_i}$. The coefficients a_i and b_i are again obtained by matching both sides of Eq. (7) up to order o (see Appendix A). A remarkable property of PPE schemes is that they preserve the unitarity of the evolution map making them ideal candidates for the simulation of quantum circuits (proof in Appendix A 2 a). A comparison of PPE and LPE schemes of different orders is provided in Fig. 1 where we show the L2-distance between the exact solution and the solution obtained from state-vector simulations Eq. (3).

F. Diagonally-exact split schemes

Learning the parameter change connecting two states via state compression is challenging. Restricting the problem to scenarios where state changes are highly localized has proven effective in mitigating this issue, easing optimization and generally improving convergence [47]. This simplification, however, usually comes at the cost of an unfavourable scaling of the number of optimizations, typically scaling with N (c.f. Section II B).

We propose to reduce the complexity of the nonlinear optimizations by splitting $\hat{\Lambda}$ as $\hat{\Lambda} = \hat{X} + \hat{Z}$, where \hat{Z} acts

diagonally in the computational basis [69] while \hat{X} is an off-diagonal matrix. The rationale will be to extract the diagonal operators which can be applied exactly to any variational parametrization.

We consider the decomposition

$$e^{\hat{\Lambda} dt} = \prod_{i=1}^s S_{\alpha_i, a_i}^{(T)} + \mathcal{O}(dt^{o(s)+1}), \quad (8)$$

where

$$S_{\alpha, a}^{(T)} = \left(\mathbb{1} + a \hat{X} dt \right) e^{\alpha \hat{Z} dt} \quad \text{with } \alpha, a \in \mathbb{C}. \quad (9)$$

The expansion is accurate to order $o(s)$ but the analytical dependence on s is not straightforward to derive. For the lowest orders we find $o(1) = 1$, $o(2) = 2$, and $o(4) = 3$. Each term in the product consists in principle of two optimizations: the first compressing the off-diagonal transformation, the second the diagonal one. The advantage of this decomposition is that the latter optimization can be performed exactly with negligible computational effort (see Appendix G).

The same approach can be extended to Padé-like schemes by substituting in Eq. (8) the term

$$S_{\alpha, b, a}^{(P)} = \left(\mathbb{1} + b \hat{X} dt \right)^{-1} \left(\mathbb{1} + a \hat{X} dt \right) e^{\alpha \hat{Z} dt}, \quad (10)$$

with $b, \alpha, a \in \mathbb{C}$. All coefficients are again obtained semi-analytically (see Appendix A). Though we do not have an explicit expression for the order $o(s)$ resulting from an s -substep expansion of this form, we find for the shallower schemes $o(1) = 2$, $o(2) = 3$, and $o(3) = 4$.

We will refer to these schemes as *splitted LPE* (S-LPE) and *splitted PPE* (S-PPE), respectively. They have the two advantages. First, they reduce the complexity of the optimizations in Eq. (4), and second, in many cases they reduce the prefactor of the error of their reciprocal non-splitted counterpart of the same order, as evidenced in Fig. 1.

III. STATE COMPRESSION OPTIMIZATIONS

In Section II, we introduced various schemes for efficiently decomposing unitary dynamics into a sequence of minimization problems, intentionally omitting the specific form of the loss function. The sole requirement was that the loss function quantify the dissimilarity between quantum states, reaching its minimum when the states perfectly match.

This section is organized as follows: In Section III A, we discuss a specific choice for the loss function — the infidelity — and explore some of its general properties. In Section III B, we review results on natural gradient optimization and introduce, in Section III C 4, an automatic regularization strategy that simplifies hyperparameter tuning for these simulations. Finally, in Section III C, we examine stochastic estimators for the fidelity and its gradient, identifying those that are most stable and perform best in practice.

A. The generic fidelity optimization problem

A common measure of similarity between two pure quantum states is the fidelity, defined as [47, 61, 70]

$$\mathcal{F}(\hat{V}|\psi\rangle, \hat{U}|\phi\rangle) = \frac{\langle \psi | \hat{V}^\dagger \hat{U} | \phi \rangle \langle \phi | \hat{U}^\dagger \hat{V} | \psi \rangle}{\langle \psi | \hat{V}^\dagger \hat{V} | \psi \rangle \langle \phi | \hat{U}^\dagger \hat{U} | \phi \rangle}, \quad (11)$$

where the operators \hat{U} and \hat{V} are included as in Eq. (4). In this work, we adopt $\mathcal{L} \equiv \mathcal{I} = 1 - \mathcal{F}$ as the loss function for each substep of Eq. (4), though alternative, less physically motivated metrics are also possible [63, 71].

The choice of operators \hat{U} and \hat{V} in Eq. (4) significantly influence the numerical complexity of the optimization. In Trotter-like decompositions, \hat{U} and \hat{V} act locally on a few particles, inducing minor changes to the wavefunctions. These localized transformations yield smoother optimization landscapes, which are effectively navigated using standard stochastic gradient methods, such as Adam [72]. This likely explains the findings of Sinibaldi et al. [47], where natural gradient optimization provided no significant improvements in performance.

In contrast, Taylor, LPE, and PPE schemes encode global transformations in \hat{U} and \hat{V} , causing the target and variational wavefunctions to diverge substantially. These global transformations result in more complex optimization landscapes, where we find standard stochastic gradient descent methods inadequate (not shown). This issue is further exacerbated when training deep neural network architectures. To address these challenges, we employ parameterization-invariant optimization strategies, specifically natural gradient descent (NGD). NGD adjusts the optimization path based on the geometry of the output space, enabling more efficient convergence in complex, high-dimensional problems. We find that NGD plays a critical role in improving both convergence and the overall efficiency of our proposed schemes.

B. Natural Gradient Descent

Let N_p be the number of parameters of the model, and N_s the number of samples used in Markov Chain Monte Carlo sampling to estimate expectation values. In its simplest implementation, given the current parameter setting $\theta_k \in \mathbb{R}^{N_p}$, NGD proposes a new iterate $\theta_{k+1} = \theta_k - \alpha_k \delta_0$, where α_k is a schedule of learning rates, and δ_0 the natural gradient at the current iterate. δ_0 is determined by minimizing a local quadratic model $M(\delta)$ of the objective, formed using gradient and curvature information at θ_k [73–75]. Formally,

$$M(\delta) = \mathcal{L}(\theta_k) + \delta^T \nabla \mathcal{L}(\theta_k) + \frac{1}{2} \delta^T \mathbf{B} \delta, \quad (12)$$

$$\delta_0 = \underset{\delta}{\operatorname{argmin}} M(\delta) = \mathbf{B}^{-1} \nabla \mathcal{L},$$

where \mathbf{B} is a symmetric positive definite *curvature matrix*. This matrix is taken to be the Fisher information matrix when modeling probability distributions, or the quantum geometric tensor (QGT) for quantum states [48, 76, 77]. The QGT is a Gram matrix, estimated as [78]

$$\mathbf{S} = E_{x \sim \pi_\psi} [\Delta J^\dagger(x) \Delta J(x)] = \mathbf{X} \mathbf{X}^\dagger \in \mathbb{C}^{N_p \times N_p}, \quad (13)$$

where $J(x) = \nabla \log \psi(x)$, $\Delta J(x) = J(x) - \mathbb{E}_{x \sim \pi_\psi} [J(x)]$, and

$$\mathbf{X} = \frac{1}{\sqrt{N_s}} [\Delta J(x_1)^\dagger | \dots | \Delta J(x_{N_s})^\dagger] \in \mathbb{C}^{N_p \times N_s}. \quad (14)$$

In essence, NGD is a way of implementing steepest descent in state space rather than parameter space. In practice, however, NGD still operates in parameter space, computing directions in the space of distributions and translating them back to parameter space before implementing the step [73, 74]. As Eq. (12) stems from a quadratic approximation of the loss, it is important that the step in parameter space be small, for the expansion (and the update direction) to be reliable. As the QGT matrix is often ill-conditioned or rank-deficient, this requirement is enforced by hand by adding to the objective a damping term with a regularization coefficient λ , penalizing large moves in parameter space. This yields the update

$$\delta_\lambda = \underset{\delta}{\operatorname{argmin}} M(\delta) + \frac{\lambda}{2} \|\delta\|^2 = (\mathbf{X} \mathbf{X}^\dagger + \lambda \mathbf{1}_{N_p})^{-1} \mathbf{X} \varepsilon, \quad (15)$$

where we used that $\mathbf{B} = \mathbf{S} = \mathbf{X} \mathbf{X}^\dagger \in \mathbb{C}^{N_p \times N_p}$ and $\nabla \mathcal{L} = \mathbf{X} \varepsilon$ with $\varepsilon \in \mathbb{C}^{N_p}$ [79]. Alternative ways of formulating this constraint exist, such as trust-region methods [75], proximal optimization, or Tikhonov damping [74], all eventually leading to Eq. (15).

It is important to note that evaluating the curvature matrix over a subset of configurations stochastically sampled from the full Hilbert space ensures at most a decrease of the loss over the sampled configurations. This

does not guarantee a reduction in the overall loss or in the loss evaluated on a different set of configurations. A desirable property of any stochastic optimization method is its ability to approach optimal (or near-optimal) behavior in the limit of infinite samples. The expectation is that, with a sufficiently large sample size, a reduction in the loss on the sampled data will correspond to a global decrease in the loss.

The main challenge with NGD is the high computational cost of inverting the QGT in large-scale models with many parameters ($N_p \gg N_s$). Various approximate approaches have been proposed to address this, such as layer-wise block diagonal approximations [80, 81], Kronecker-factored approximate curvature [82, 83], and unit-wise approximations [84, 85]. At the moment, the only method enabling the use of NGD in deep architectures without approximating the curvature matrix is the tangent kernel method [86, 87], recently rediscovered in the NQS community as minSR [88]. This approach leverages a simple linear algebra identity [86, 89, 90] to rewrite Eq. (15) as

$$\delta_\lambda = \mathbf{X}(\mathbf{X}^\dagger \mathbf{X} + \lambda \mathbf{1}_{N_s})^{-1} \varepsilon, \quad (16)$$

where the matrix $\mathbf{T} = \mathbf{X}^\dagger \mathbf{X} \in \mathbb{C}^{N_s \times N_s}$ is known as the *neural tangent kernel* (NTK) [91, 92]. In the limit where $N_p \gg N_s$, the NTK becomes much more tractable than the QGT, shifting the computational bottleneck on the number of parameters to the number of samples.

C. Stochastic estimators

Estimators of the fidelity [Eq. (11)] take the general form

$$\mathcal{F}(|\psi\rangle, |\phi\rangle) = \mathbb{E}_{(x,y) \sim \chi} [f(x,y)], \quad (17)$$

for a suitable choice of random variable σ , sampling distribution $\chi(\sigma)$, and local estimator $f(\sigma)$. While this expression is exact, its direct evaluation incurs exponential scaling with system size N , rendering it computationally infeasible. Equation (18) is thus generally approximated by its sample mean

$$\bar{f}_{N_s} = \frac{1}{N_s} \sum_{i=1}^{N_s} f(x_i, y_i) \quad \text{with} \quad (x_i, y_i) \sim \chi, \quad (18)$$

evaluated over a number of samples N_s scaling polynomially in system size.

Importantly, different stochastic estimators, while sharing identical expectation values in the limit of infinite samples, can exhibit significantly different behavior over finite sample sizes. Though some attention has been given to characterizing the properties of different fidelity estimators [47], a systematic study of the variance properties of the estimators of the gradient is still lacking. As an accurate estimation of the gradient is crucial for driving fidelity optimization to convergence, this represents a central issue for quantum many-body dynamics.

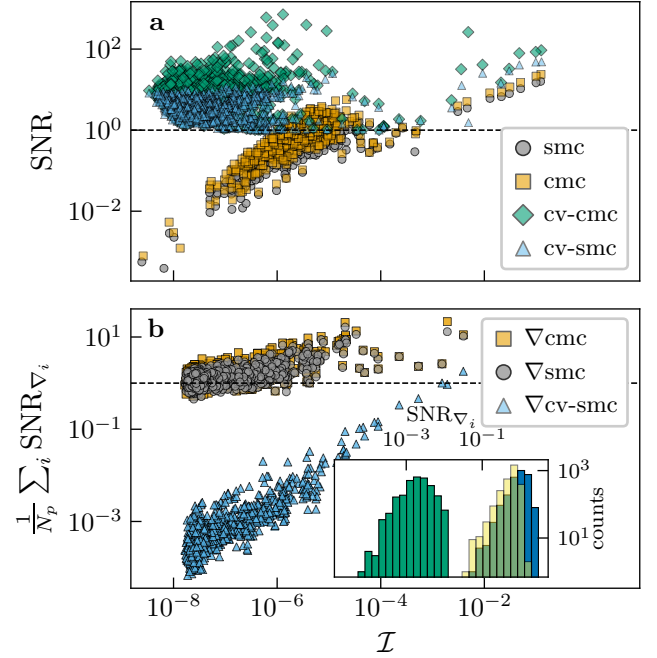


FIG. 2. (a) Signal-to-noise ratio [Eq. (20)] of the infidelity as a function of its exact value for the estimators given in Eqs. (19) (smc), (22) (cmc), (21) (cv-smc), and (23) (cv-cmc). For all control-variate-enhanced estimators, the control coefficient is set to the asymptotically optimal value $c = -1/2$. (b) Component-averaged signal-to-noise ratio of the infidelity gradient estimators in Eqs. (26) (∇cmc), (25) (∇smc), and (27) ($\nabla\text{cv-smc}$). The inset shows the distribution of the component-wise signal-to-noise ratio at the 300-th iterate. All estimators are evaluated on the same states, specifically those visited along the curve with lowest final infidelity among those reported in Fig. 3(a). Parameters: $N = 16$, $J = 1$, $h = h_c/10$, $N_s = 2^{12}$, $n_{\text{iter}} = 10^3$, $\alpha = 0.27$, $\lambda = 3.17 \times 10^{-7}$, and $\Theta_{\text{CNN}} = (10, 10, 10, 10; 3)$.

In Section III C 1 we extend the analysis of Sinibaldi et al. [47], further improving on the variance properties of the fidelity estimator. In Section III C 2 we examine the properties of various gradient estimators, decoupling their analysis from that of the fidelity itself. Our findings are summarized in Tables II and III, respectively.

1. Fidelity

As explained in Ref. [70], the natural choice for the fidelity estimator in Eq. (18) is the *simple Monte Carlo* (smc) estimator defined by

$$\begin{aligned} \chi(x,y) &= \pi_\psi(x)\pi_\phi(y) \equiv \pi(x,y), \\ f(x,y) &= \frac{\phi(x)\psi(y)}{\psi(x)\phi(y)} \equiv A(x,y), \end{aligned} \quad (19)$$

where the samples $\sigma = (x,y)$ are drawn from the joint Born distribution $\pi(x,y)$ of the two states. Since $\pi(x,y)$

Name	Ref.	Eq.	+CV	+RW
smc	[47], III C 1	(19)	(21)	(E1)
cmc	[60–62], III C 1	(22)	(23)	(E3)

TABLE II. List of stochastic fidelity estimators, their definition, and their expression with control variables (CV) and reweighting (RW). +CV links to the expressions of the estimators with control variables. +RW links to the expressions allowing sampling from the Born distribution of $|\phi\rangle$ rather than $\hat{U}|\phi\rangle$ when linear transformations are applied to the target or variational state. Figure 2 shows that both estimators perform similarly, and need CV to give accurate values.

is separable, sampling can be carried out independently over the Born distributions $\pi_\psi(x) = |\psi(x)|^2 / \langle \psi | \psi \rangle$ and $\pi_\phi(y) = |\phi(y)|^2 / \langle \phi | \phi \rangle$. While Ref. [70] demonstrated that the variance of this estimator scales polynomially with system size, it does not vanish as $\mathcal{F} \rightarrow 1$ and is therefore an unreliable indicator of progress in state compression problems [47]. In Fig. 2(a), we provide evidence of this by displaying the estimator’s signal-to-noise ratio (SNR)

$$\text{SNR} = \sqrt{\frac{|\bar{f}_{N_s}|^2}{\frac{N_s}{N_s-1} \sum_{i=1}^{N_s} |f^2(\sigma_i) - \bar{f}_{N_s}|^2}} \quad (20)$$

as a function of the exact infidelity recorded along the best optimization amongst those presented in Fig. 3(a).

To address the vanishing SNR of the smc estimator, Sinibaldi et al. [47] leveraged the identity $\mathbb{E}_\pi[|A(x, y)|^2] = 1$ to construct the *control-variate-enhanced smc* (cv-smc) estimator

$$\begin{aligned} \chi(x, y) &= \pi(x, y) \\ f(x, y) &= \text{Re}\{A(x, y)\} + c(|A(x, y)|^2 - 1) \equiv F(x, y). \end{aligned} \quad (21)$$

As shown in Fig. 2(a), the use of the analytical control variable $|A(x, y)|^2$ allows for drastic variance reduction upon appropriate tuning of the control parameter c [93].

An alternative variance reduction technique, readily applicable to Eq. (19), is Rao-Blackwellization. In its simplest form, Rao-Blackwellization reduces the variance of an estimator by replacing it with the conditional expectation with respect to a subset of its variables [94, 95]. For the particular case of a distribution that can be factorized such as $\chi(x, y) = \pi_\psi(x)\pi_\phi(y)$, Rao-Blackwellization amounts to marginalizing over the target state’s distribution. In the following, we will refer to the Rao-Blackwellized smc estimator as the *conditional Monte Carlo* (cmc) estimator, expressed as (details in

Name	Ref.	Eq.	+RW	NTK	Stability
∇cmc	[60–62], III C 2	(26)	(E3)	✓	High
∇smc	III C 2	(25)	(E1)	✓	Medium
$\nabla\text{cv-smc}$	[47, 53]	(27)	(E1)	✗	Low

TABLE III. List of estimators for the gradient of the infidelity. The NTK column lists the equation to implement the natural gradient estimator in the limit of large number of parameters. Not all estimators can be expressed that way. +RW links to the expressions allowing sampling from the Born distribution of $|\psi\rangle$ rather than $\hat{V}|\psi\rangle$ when linear transformations are applied to the target or variational state. The stability score is determined by the empirical results discussed in Fig. 3.

Appendix D

$$\begin{aligned} \chi(x, y) &= \chi(x) = \pi_\psi(x), \\ f(x) &= \mathbb{E}[A(x, y)|x] = A_x(x) \mathbb{E}_{y \sim \pi_\phi}[A_y(y)] \equiv H_{\text{loc}}(x), \end{aligned} \quad (22)$$

where $A(x, y) = A_x(x)A_y(y)$, with $A_x(x) = \phi(x)/\psi(x)$ and $A_y(y) = \psi(y)/\phi(y)$. Within this framework, the fidelity can be interpreted as the expectation value of the projector $\hat{H} = |\phi\rangle\langle\phi| / \langle\phi|\phi\rangle$ over the state $|\psi\rangle$ [96].

We remark that the computational cost of both Eqs. (19) and (22) is equivalent. Indeed, they use the same set of samples $\{(x_i, y_i)\}_{i=1}^{N_s}$ and evaluate ψ and ϕ over all of them. The difference is that while Eq. (19) sums over the diagonal pairs (x_i, y_i) alone, the sample average in Eq. (22) includes all cross terms (x_i, y_j) .

Though the connection to conditional Monte Carlo was not drawn, the cmc estimator was used in Refs. [60–62]. We demonstrate in Fig. 2(a) that just like the smc estimator, the cmc estimator also suffers from a vanishing SNR in the limit of $\psi \rightarrow \phi$.

In the following, we combine the two variance reduction techniques detailed above, control variates and Rao-Blackwellization, to produce the *control-variate-enhanced cmc* (cv-cmc) estimator (derivation in Appendix B)

$$\begin{aligned} \chi(x) &= \pi_\psi(x) \\ f(x) &= \mathbb{E}[F(x, y)|x] \\ &= \text{Re}\{H_{\text{loc}}(x)\} + c(|A_x(x)|^2 \mathbb{E}_{y \sim \pi_\phi}[|A_y(y)|^2] - 1). \end{aligned} \quad (23)$$

As a direct consequence of the Rao-Blackwell theorem, the cv-cmc estimator displays an SNR performance superior to all others, as illustrated in Fig. 2(a). We adopt this estimator in all simulations presented below.

We finally remark that, as discussed in Section II, p-tVMC often requires evaluating $\mathcal{F}(\hat{V}|\psi), \hat{U}|\phi\rangle$. Although this might appear to implicate the necessity of sampling from the Born distributions of the transformed states $\hat{V}|\psi\rangle$ and $\hat{U}|\phi\rangle$, we show in Appendix E the possibility of sidestepping this complexity by means of im-

portance sampling.

2. Gradient

While the preceding section provides compelling evidence that control variates are essential for accurate fidelity estimation, it does not address how this impacts the estimation of the gradient. In gradient-based optimization problems, such as Eq. (4), managing the variance of gradient estimates is crucial for achieving stable and efficient convergence. Historically, however, implementations of infidelity-optimization strategies have overlooked this aspect, simply adopting the gradient estimator obtained from automatic differentiation of the chosen fidelity estimator according to:

$$\begin{aligned}\nabla\mathcal{F} &= \nabla\mathbb{E}_\chi[f(\sigma)] = \mathbb{E}_\chi[g(\sigma)], \\ g(\sigma) &= 2\operatorname{Re}\{\Delta J(\sigma)\}f(\sigma) + \nabla f(\sigma).\end{aligned}\quad (24)$$

While for an infinite number of samples, this expression is of course valid, when approximating the average with the sample mean \bar{g}_{N_s} , there is no guarantee that the selected gradient estimator will perform well. Indeed, as we show below, good variance properties of the fidelity estimator do not necessarily translate, under Eq. (24), into good variance properties of the gradient estimator. As a result, stable low-variance estimators for both fidelity and gradient have, until now, never been employed simultaneously. Specifically, while Refs. [47, 53] employ a control-variate-enhanced estimator for the fidelity, their choice of gradient estimator suffers from a vanishing SNR, rendering it ineffective for optimization. Conversely, the gradient estimator adopted in Refs. [60–62] has good variance properties, while the fidelity estimator exhibits a vanishing SNR. We observe this often leads to an underestimation of the quality of the results.

In support to this point, we explicitly evaluate the gradient estimators obtained from the smc, cmc, and cv-smc fidelity estimators, and compare their performance. We refer to such estimators as ∇smc , ∇cmc , and $\nabla\text{cv-smc}$, respectively. For the smc estimator [Eq. (19)], automatic differentiation yields:

$$\begin{aligned}\chi(x, y) &= \pi(x, y), \\ g(x, y) &= 2\operatorname{Re}\{\Delta J(x)A(x, y)^*\},\end{aligned}\quad (25)$$

with $\Delta J(x)$ defined in Eq. (13). Applying the same procedure to the cmc estimator [Eq. (22)] results in:

$$\begin{aligned}\chi(x, y) &= \chi(x) = \pi_\psi(x), \\ g(x, y) &= 2\operatorname{Re}\{\Delta J(x)H_{\text{loc}}(x)^*\}.\end{aligned}\quad (26)$$

This choice underlies the investigations in Refs. [60–62]. Notably, the expression in Eq. (26) can be derived directly via Rao-Blackwellization of Eq. (25), guaranteeing a reduction in variance. Finally, the gradient obtained by

differentiation of the cv-smc estimator [Eq. (21)] reads:

$$\begin{aligned}\chi(x, y) &= \pi(x, y), \\ g(x, y) &= \operatorname{Re}\left\{2\Delta F(x, y)J(x) + \left(A(x, y) + 2c|A(x, y)|^2\right)[J(y) - J(x)]\right\},\end{aligned}\quad (27)$$

with $F(x, y)$ as defined in Eq. (21). This expression underlies the studies in Refs. [47, 53].

To evaluate the performance of these gradient estimators, we first compare their SNRs. Since $\nabla\mathcal{F} \in \mathbb{R}^{N_p}$, we compute the SNR of each component of the gradient vector. In Fig. 2(b), we present the component-averaged SNR as a function of the true infidelity recorded during the best optimization run of Fig. 3(a). The inset shows a distribution of per-component SNR values. Interestingly, while the cv-smc estimator achieves superior SNR for fidelity estimation, this advantage is reversed when estimating the gradient. Specifically, the SNR of the cv-smc gradient estimator declines rapidly as the simulation progresses toward convergence. In contrast, gradient estimators derived from the bare smc and cmc fidelity estimators maintain an SNR on the order of $\mathcal{O}(1)$ as convergence is approached. We attribute this disparity to the covariance structure present in Eqs. (25) and (26), but absent in Eq. (27). This covariance structure introduces sample-specific control variates that dynamically adapt to the non-stationary nature of the variables, significantly reducing variance and enhancing estimator stability (c.f. Appendix D).

To further characterize the performance of the gradient estimators, we examine their ability to drive infidelity optimizations to convergence. As a benchmark, we consider a state-matching problem in which we optimize the variational state to match a given reference state. As a physical reference we take $|\psi(t)\rangle = \exp(-i\hat{H}t)|\rightarrow \dots \rightarrow\rangle$ with \hat{H} the transverse field Ising Hamiltonian in Eq. (32). In general, we observe that states at shorter times are easier to learn, with smaller differences in the results produced by the various gradient estimators. Conversely, states at longer times are significantly more challenging to accurately match. It is important to emphasize that this state-matching setup is inherently more demanding than the dynamics itself. In the simulation of dynamics, the state at each timestep is initialized from the preceding timestep, offering a more informed starting point closer to the target state. By contrast, the state-matching problem begins in general from a random state, making the optimization considerably more difficult.

In Fig. 3 we present the accuracies with which we were able to recover the state at $Jt = 0.5$, a time point that we consider *relatively challenging* and representative of the general trends observed. Convergence is quantified by the final optimization infidelity (colormap) which we display as a function of the regularization parameter λ and learning rate α for the different gradient estimators detailed above. For each pair (α, λ) we consider 10 different replicas with different sampling histories. Black

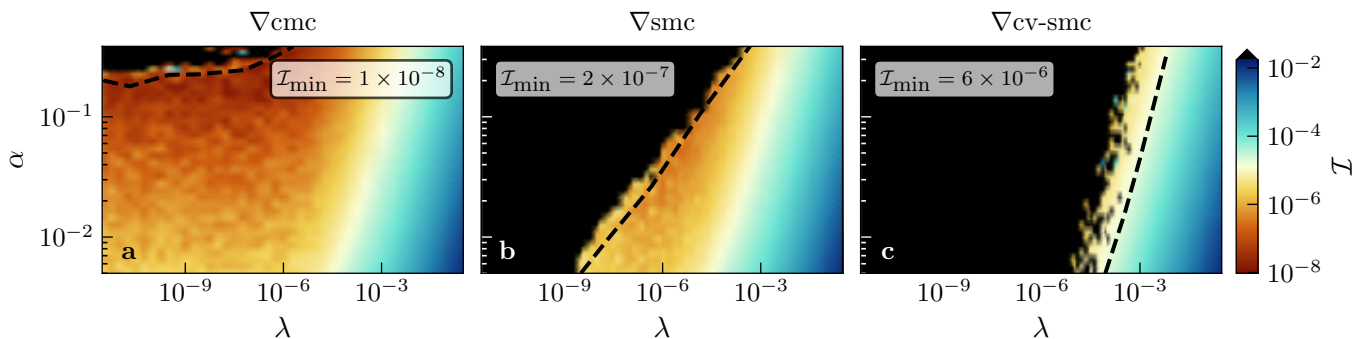


FIG. 3. Stability diagram for the (a) ∇cmc [Eq. (26)], (b) ∇smc [Eq. (25)], and (c) $\nabla\text{cv-smc}$ [Eq. (27)] gradient estimators as a function of the regularization coefficient λ and learning rate α . Stability is quantified by the lowest infidelity (color scale) achieved across an ensemble of 10 optimizations with identical hyperparameters, identical initial parameters, but different random seeds for the Monte Carlo sampling. Comparisons are made for a fixed computational cost as all optimizations consist of $n_{\text{iter}} = 10^3$ iterations. Analogous conclusions can be drawn from the stability diagrams where $n_{\text{iter}}/\alpha = \text{const.}$ (not shown). Regions in black correspond to (α, λ) combinations where all simulations diverged, indicating instability. Dashed black lines outline areas where more than 50% of simulations diverged, providing a second visual stability threshold supporting the stability summary in Table III. The inset in each panel shows the minimal infidelity \mathcal{I}_{min} achieved within the stable region (fewer than 50% of simulations diverged). For reliability and consistency, regardless of the chosen gradient estimator, we display the exact fidelity evaluated in full-summation. While the reference state wave function is exactly encoded into the parameters of a log-state-vector ansatz, the variational state is approximated with a complex CNN architecture. Parameters: $N = 16$, $J = 1$, $h = h_c/10$, $N_s = 2^{12}$, $n_{\text{iter}} = 10^3$, and $\Theta_{\text{CNN}} = (10, 10, 10, 10; 3)$.

regions in the figure represent instability zones, where all replicas diverged, indicating poor stability of the method for the selected hyperparameter combination.

Overall, our results indicate that the ∇cmc gradient estimator consistently delivers the best convergence and exhibits the highest stability among all the gradient estimators examined in this study and reported in the available literature. We rely on this estimator for all optimizations presented in Section IV.

3. Large number of parameters (NTK) limit

As discussed in Section III B, when computing the natural gradient for large models with more than a few tens of thousands of parameters, inverting the QGT becomes intractable. In such cases it becomes necessary to use the NTK. This reformulation of the natural gradient is only possible if the gradient estimator takes the form $\nabla\mathcal{F} = \mathbf{X}\varepsilon$, with $\mathbf{X} \propto \Delta J^\dagger$ as defined in Eq. (14). This, however, is not a prerogative of all estimators. Specifically, while the ∇smc and ∇cmc estimators admit such decomposition with, respectively, $\varepsilon = (A(x_1, y_1), \dots, A(x_N, y_N))$ and $\varepsilon = (H_{\text{loc}}(x_1), \dots, H_{\text{loc}}(x_N))$, the $\nabla\text{cv-smc}$ estimator does not. This restriction prevents these estimators from being efficiently computed in the NTK framework, making them a poor choice for scaling to the deep network limit.

In addition to not supporting NTK, the absence of a form like $\nabla\mathcal{F} = \mathbf{X}\varepsilon$ also precludes the use of L-curve and generalized cross-validation methods for adaptively selecting the regularization coefficient λ . While these automatic damping strategies have been used in the litera-

ture [97], they are less suited to the NGD problem compared to those discussed in Section III C 4.

4. Autonomous damping

Choosing an appropriate value for λ is crucial for successful optimization. If λ is too large, the update resembles standard gradient descent with a very small learning rate. Conversely, if λ is too small, updates can become excessively large, particularly in low-curvature directions, possibly leading to increasing the loss rather than decreasing it [73]. Identifying an optimal value for λ is non-trivial, and it is rare for a single value of λ to be suitable across all optimization iterations. This challenge is exacerbated in p-tVMC calculations, where numerous successive infidelity optimizations, with very different target and initial states, must be performed. Performing an hyperparameter search analogous to that in Fig. 3 for every state compression is of course impractical, and an automated approach is required. Hereunder, we introduce a custom adaptive control strategy inspired by heuristics commonly employed in the numerical optimization literature [73–75, 82, 98].

Let θ_k be the parameters at the k -th iterate. The parameters at the following iterate are $\theta_{k+1} = \theta_k + \delta\theta_k$ with $\delta\theta_k = -\alpha_k \delta_{\lambda_k}$. Here, δ_{λ_k} is the natural gradient update, and α_k is the learning rate. Under ideal conditions (accurate curvature matrix, infinite sample size, and proper regularization), the optimal learning rate $\alpha_k = 1$ maximizes the decrease of the quadratic model. However, these conditions are rarely satisfied in practice and mitigating the overfitting caused by finite-sample effects typ-

ically requires lowering α_k [73]. We find that $\alpha_k \gtrsim 0.1$ is a reasonable choice in most cases.

To dynamically adapt λ_k , we build on the Levenberg-Marquardt heuristic, which relies on the reduction ratio

$$\rho_k = \frac{\mathcal{L}(\theta_k + \delta\theta_k) - \mathcal{L}(\theta_k)}{M(\delta\theta_k) - \mathcal{L}(\theta_k)}. \quad (28)$$

This ratio measures the accuracy of the quadratic model $M(\delta\theta_k)$ [c.f. Eq. (12)] in predicting $\mathcal{L}(\theta_k + \delta\theta_k)$. Small ρ_k suggests poor agreement between the model and the actual loss, indicating the need to increase λ_k . Larger ρ_k indicates good agreement, allowing λ_k to be reduced [99]. The standard Levenberg-Marquardt algorithm aims at keeping $1/4 \leq \rho_k \leq 3/4$ by taking $\lambda_{k+1} = m_k \lambda_k$ with

$$m_k = \begin{cases} 3/2 & \text{if } \rho_k \leq \frac{1}{4} \\ 2/3 & \text{if } \rho_k > \frac{3}{4} \\ 1 & \text{if } \frac{1}{4} < \rho_k \leq \frac{3}{4} \end{cases}. \quad (29)$$

Steps where $\rho_k < 0$ (loss increases) are discarded and recomputed with the adjusted λ_k .

While effective in many cases, the standard heuristic can result in rapid and uncontrolled variations in ρ_k and λ_k , leading to suboptimal performance. Drawing inspiration from step-size control in differential equations, we enhance this heuristic by incorporating proportional-integral controllers, which enhance stability by combining proportional responses to current errors with integral corrections from accumulated past errors [100]. As a measure of the error we take the deviation of ρ_k from a desired target value ρ^* . The multiplier m_k for adjusting λ_k is then taken to be

$$m_k = \gamma_s \min \left[e_{\max}, \max \left[e_{\min}, E^{\beta_1}(\rho_k) E^{-\beta_2}(\rho_{k-1}) \right] \right], \quad (30)$$

where γ_s is a safety factor to favor acceptable error levels in subsequent steps, e_{\min} and e_{\max} constrain the scaling factor within a safe range, and β_1 and β_2 control the influence of current and past errors, respectively. Contrary to standard controllers where the magnitude of the (positive) error alone modulates m_k , here the sign of the error plays an important role as well. Specifically, the error functional $E(\rho)$ is chosen to ensure that $m_k > 1$ for $\rho_k < \rho^*$ and $m_k < 1$ for $\rho_k > \rho^*$. While various choices are possible, we choose

$$E(\rho) = \text{sgn}(\rho^* - \rho) |\rho^* - \rho|^q + 1, \quad (31)$$

which which we display as an inset to Fig. 4(a). To further enhance robustness, we reject steps where $\rho_k > \rho_{\max}$ or $\rho_k < \rho_{\min}$ and recompute the update with the newly adjusted λ_k .

We find the proposed approach to work well in practice and to be insensitive to minor changes in the selected thresholds. For the latter we find $q = 3$, $\beta_1 = 0.66$, $\beta_2 = 0.33$, $\alpha = 0.3$, $\rho_{\max} = 3$, $\rho_{\min} = 0.1$, $\rho^* = 0.75$, $\gamma_s = 0.9$, $e_{\max} = 2$, and $e_{\min} = 0.05$ to be good choices.

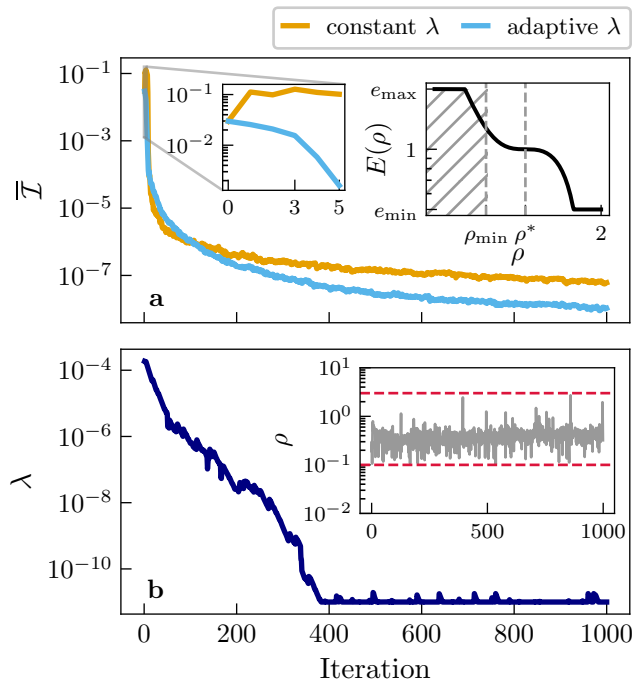


FIG. 4. Performance of the autonomous damping algorithm described in Eq. (30). (a) Comparison of the infidelity across the optimization. The infidelity is computed exactly and averaged over 10 Monte Carlo runs, with parameter updates derived from noisy estimates of the ∇_{vmc} gradient and curvature matrix. Results are compared to the best configuration ($\alpha = 0.27$, $\lambda = 3 \times 10^{-7}$) from Fig. 3(a). The first inset highlights an initial increase in the loss due to a suboptimal initial choice of λ . The second inset characterizes the behavior of the error function $E(\rho)$ in Eq. (31). Hatching is used to highlight the region $\rho < \rho_{\min}$ where updates are discarded and recomputed. (b) Evolution of the diagonal shift. The data corresponds to the replica achieving the lowest infidelity. The inset displays the value of reduction ratio ρ at each substep. Parameters: $q = 3$, $\beta_1 = 0.66$, $\beta_2 = 0.33$, $\alpha = 0.3$, $\rho_{\max} = 3$, $\rho_{\min} = 0.1$, $\rho^* = 0.75$, $\gamma_s = 0.9$, $e_{\max} = 2$, and $e_{\min} = 0.05$.

IV. NUMERICAL EXPERIMENTS

In the following sections, we benchmark our methods on the paradigmatic example of the two-dimensional transverse-field Ising model (TFIM), a widely used testbed for NQS dynamics [24, 47, 49, 50, 59, 63]. The Hamiltonian is given by

$$\hat{H} = -J \sum_{\langle i,j \rangle} \hat{\sigma}_i^z \hat{\sigma}_j^z - h \sum_i \sigma_i^x, \quad (32)$$

where J is the nearest-neighbor coupling strength and h represents the transverse field strength. Throughout this work, we set $J = 1$, we adopt periodic boundary conditions, and we fix the z -axis as the quantization axis.

At zero temperature, this model undergoes a quantum phase transition at the critical point $h_c = 3.044$. This separates the ferromagnetic phase ($h < h_c$), from the

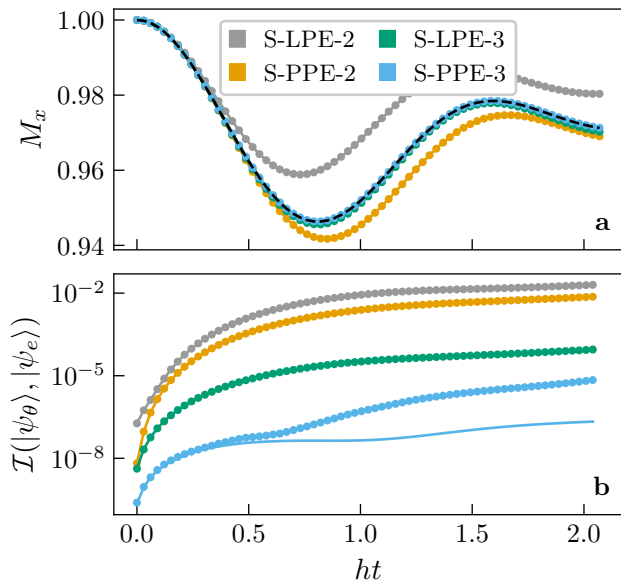


FIG. 5. Quench dynamics ($h = \infty \rightarrow 2h_c$) of the transverse-field Ising model on a 4×4 lattice obtained using different integration schemes: S-LPE-2, S-LPE-3, S-PPE-2, S-PPE-3. We show the evolution of the average magnetization M_x (a), and of the infidelity between the exact solution $|\psi_e\rangle$ and its variational approximation $|\psi_\theta\rangle$ (b). Full dots are used to mark variational data, obtained by solving the optimization problems in Eq. (4). Solid lines detail the ideal behavior of each integrator scheme, estimated from a full full state-vector simulation of the dynamics resulting from the product expansion of the evolver. Parameters: $N = 16$, $J = 1$, $h = 2h_c$, $N_s = 2^{14}$, $\Theta_{\text{CNN}} = (5, 4, 3; 3)$, and $dt = 0.025$.

paramagnetic phase ($h > h_c$). Deep in the ferromagnetic phase ($h \rightarrow 0$) the ground state is degenerate and lies in the subspace spanned by $|\uparrow \dots \uparrow\rangle$ and $|\downarrow \dots \downarrow\rangle$. In the opposite limit ($h \rightarrow \infty$), the ground state is $|\rightarrow \dots \rightarrow\rangle$, with spins aligned along the transverse field direction.

We demonstrate that the far-from-equilibrium dynamics characteristic of the quantum quenches of this model can be efficiently captured using p-tVMC. Our results are consistent across architectures, integration schemes, and quench parameters.

A. Small-scale experiments

Before presenting results for large system sizes, we validate our method against exact diagonalization results on a 4×4 lattice: small enough to allow simulating the exact dynamics but large enough for MC sampling to be non-trivial. We consider the quench dynamics in which the system is initialized in the paramagnetic ground state at $h = \infty$, and evolved under a finite transverse field of strength $h = 2h_c$. For these simulations we adopt the Convolutional Neural Network (CNN) ansatz described in Appendix H 1.

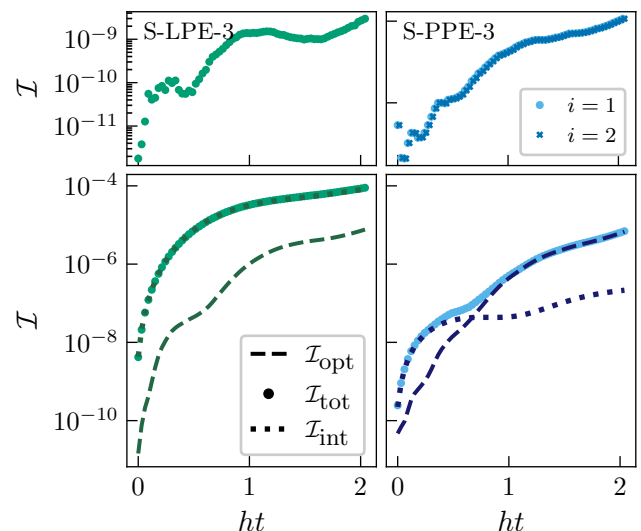


FIG. 6. Evolution of the total infidelity (\mathcal{I}_{tot}), integration infidelity (\mathcal{I}_{int}), and optimization infidelity (\mathcal{I}_{opt}) as a function of time. The exact dynamics $|\psi_e(t)\rangle$, the dynamics obtained from state-vector simulations of product schemes $|\psi_a(t)\rangle$, and the variational dynamics $|\psi_\theta(t)\rangle$ are compared. The infidelities are defined as follows: $\mathcal{I}_{\text{tot}} = \mathcal{I}(|\psi_e(t)\rangle, |\psi_\theta(t)\rangle)$, $\mathcal{I}_{\text{int}} = \mathcal{I}(|\psi_e(t)\rangle, |\psi_a(t)\rangle)$, and $\mathcal{I}_{\text{opt}} = \mathcal{I}(|\psi_a(t)\rangle, |\psi_\theta(t)\rangle)$. The final step infidelities obtained at the end of the optimization problems in Eq. (4) are reported in the top panels. The different substeps of the S-PPE-3 scheme are indexed by i . Parameters: same as in Fig. 5.

We compare several integration schemes: S-LPE-3, S-PPE-3 (third-order in dt), and S-LPE-2, S-PPE-2 (second-order in dt). We intentionally choose a fixed step size of $hdt = 3 \times 10^{-2}$, too big for product schemes of second order to accurately approximate the dynamics at hand, to underscore the advantages of our higher-order schemes. Optimizations are performed using NGD and the autonomous damping strategies detailed in Section III C 4.

The variational evolution closely follows the expected behavior of the integration scheme, achieving infidelities from the exact solution below 10^{-5} for the best-performing S-PPE-3 scheme. The expected behaviour of each integrator is estimated by applying the product expansion to the full state vector [equivalent to solving exactly the optimization problem in Eq. (4) on a log-state vector ansatz]. By doing so, we observe that the variational dynamics is influenced by two sources of error: optimization error and integration error. In the absence of optimization error, the variational dynamics would follow the approximate integrator's dynamics which, in the absence of integration error, would in turn match the exact evolution. For most schemes presented in Fig. 5, the dynamics is dominated by the integration error, except for S-PPE-3, where the discretization scheme is sufficiently accurate for the optimization error to become dominant at $ht \gtrsim 0.6$.

The crossover between integration and optimization errors is more apparent in Fig. 6, where we analyze the error sources affecting S-LPE-3 and S-PPE-2, the two best-performing schemes. While S-LPE-3 is dominated by integration error, S-PPE-3 shows a crossover point where optimization error begins to dominate, as indicated by the intersection of the dashed and dotted lines.

B. Large-scale experiments

We now demonstrate the effectiveness of our methods for simulating large-scale quantum dynamics. We again focus on the quench dynamics of the TFIM, this time on a 10×10 lattice and for the more challenging quench from $h = \infty$ to $h = h_c/10$.

While no exact solution is available at this scale, this problem is widely used as a benchmark in quantum dynamics, allowing for comparison with established methods. In Fig. 7, we present results obtained using the S-LPE-3 integration scheme (c.f. Section II F) for times up to $Jt = 2$ where comparison with existing results is meaningful.

To rigorously evaluate our approach, we utilize two architectures: a CNN with configuration $\Theta_{\text{CNN}} = (5, 4, 3; 6)$ to explore the regime $N_s \gg N_p$, and a Vision Transformer (ViT) with $\Theta_{\text{ViT}} = (2, 12, 6, 4; 6)$ for the opposite case where $N_s \ll N_p$. In the latter regime, direct inversion of the QGT becomes prohibitively expensive and the gradient estimator introduced in Eq. (26) proves essential for the evaluation of the natural gradient. As shown in Fig. 7(a), both models provide consistent predictions, underscoring the effectiveness of p-tVMC in yielding consistent results across different architectures, provided they are sufficiently expressive. These findings establish the ViT as a promising ansatz not only for ground-state simulations, as previously shown in Refs. [39, 102], but also for large-scale simulations of quantum dynamics.

While the p-tVMC results, the iPEPS data from Ref. [101], and the largest tVMC simulations from Ref. [49], generally show strong agreement, subtle differences emerge around the more challenging region $Jt \gtrsim 1.4$. Here, the tVMC curves deviate from the iPEPS predictions, while p-tVMC maintains closer alignment, suggesting superior stability at longer times. This is further quantified in Fig. 7(b), where we report the absolute deviation from the iPEPS baseline. Notably, p-tVMC captures long-time dynamics more accurately, highlighting its potential for enhanced long-term stability. We further observe, at the early stages of the simulation ($0.1 \lesssim Jt \lesssim 0.4$), the existence of a small region where tVMC data are marginally better aligned with the iPEPS baseline compared to p-tVMC. This region coincides with the high-activity region of the adaptive timestepping algorithm used in the tVMC simulations suggesting the origin of this discrepancy to be found in the larger, fixed, timestep employed in our calculations. While our current

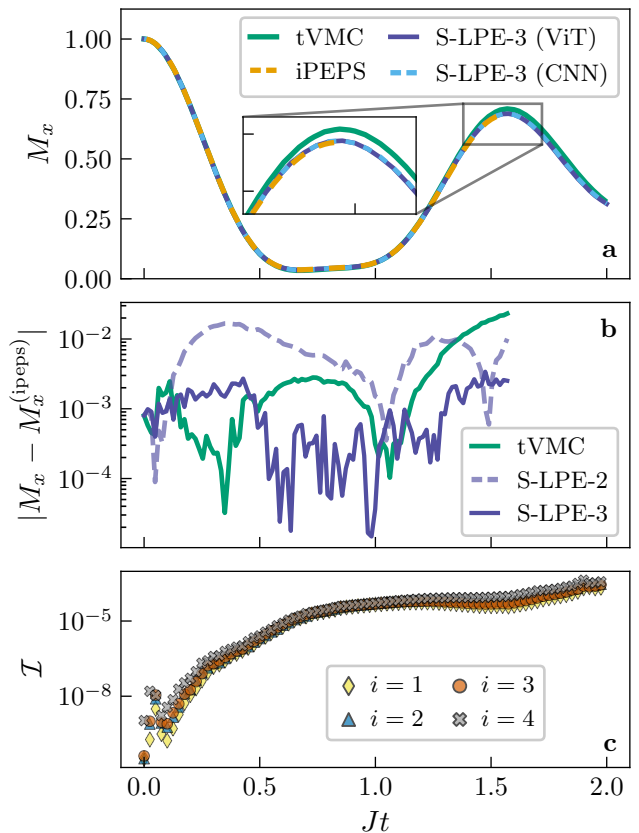


FIG. 7. Quench dynamics across the critical point of the TFIM ($h = \infty \rightarrow h_c/10$) on a 10×10 lattice. (a) Average magnetization as a function of time. Results are compared with existing methods: tVMC [49] and iPEPS [101]. P-tVMC simulations are obtained using the S-LTE-3 scheme on two architectures: CNN and ViT. (b) Absolute difference in average magnetization between the iPEPS baseline and the variational simulations. P-tVMC results obtained using the SLPE2 and SLPE3 schemes are displayed. (c) Final optimization infidelity (step infidelity) achieved at each substep $i = 1, \dots, 4$ of the S-LTE-3 scheme. For clarity, in panels (b) and (c) only the results for the ViT architecture are displayed. Similar curves were observed with the CNN (not shown). Parameters: $N = 100$, $J = 1$, $h = h_c/10$, $N_s = 2^{17}$ (CNN), $\Theta_{\text{CNN}} = (5, 4, 3; 6)$, $N_s = 2^{15}$ (ViT), $\Theta_{\text{ViT}} = (2, 12, 6, 4; 6)$, and $dt = 0.025$.

results are competitive with state-of-the-art methods, implementing adaptive timestepping in future iterations will further enhance the overall accuracy of the results. Finally, in Eq. (32)(c) we display the final step-infidelities at each time step. We attribute the degradation in the quality of the fidelity optimisations to finite-sample effects that become more pronounced at later times. To validate this hypothesis we ran the same optimisations in a smaller 4×4 lattice in full summation, observing a convergence to numerical precision (see Appendix F).

We remark that to stabilize our simulations, we employed the autonomous damping strategy outlined in

Section III C 4. All systems were initialized using a robust two-step process where we first use traditional VMC to approximate the ground state of $\hat{H}x = \sum_i \hat{\sigma}_i^x$, and then perform infidelity minimization to align the variational state with the constant-amplitude target state $\phi_{\text{gs}}(y) = \text{const. for all } y \in [-1, +1]^N$.

V. CONCLUSIONS AND OUTLOOKS

In this work, we provide a rigorous formalization of the p-tVMC method, decoupling the discretization of time evolution from the state compression task, performed by infidelity minimization.

In our analysis of the discretization scheme, we identify key criteria for constructing schemes that are simultaneously accurate and computationally efficient. Building on these principles, we address the limitations in prior approaches to p-tVMC through two novel families of integration schemes capable of achieving arbitrary-order accuracy in time while scaling favorably with the number of degrees of freedom in the system. This is made possible by making efficient use of the specific structure of the p-tVMC problem.

In the study of the fidelity optimization, we demonstrate the critical role of natural gradient descent in compressing non-local transformations of the wavefunction into parameter updates. Additionally, we introduce an automatic damping mechanism for NGD which provides robust performance without the need for extensive hyperparameter tuning at each timestep of the dynamics.

We further clarify which among the available stochastic estimators are most reliable for computing both the infidelity and its gradient, addressing open questions regarding the role of control variates in the estimation of infidelity and their necessity in gradient-based optimization.

By integrating these advances into the p-tVMC framework, we demonstrate the potential to achieve machine precision in small-scale state compression and time evolution tasks. Applying these methods to larger systems, we show that p-tVMC not only reproduces state-of-the-art tVMC results with higher accuracy and improved control, but also surpasses previous methods in terms of generality and stability.

While fully numerically exact simulations on large systems remain beyond reach — likely due to limitations in Monte Carlo sampling — this work establishes p-tVMC as a highly promising approach, capable of overcoming several intrinsic challenges faced by other methods, and bringing us closer to achieving precise, large-scale classical quantum simulations.

SOFTWARE

Simulations were performed with NetKet [103, 104], and at times parallelized with mpi4JAX [105]. This

software is built on top of JAX [106], equinox [107] and Flax [108]. We used QuTiP [109, 110] for exact benchmarks. The accompanying code and Mathematica scripts for the manuscript are available at github.com/NeuralQXLab/ptvmc-systematic-study.

ACKNOWLEDGMENTS

We acknowledge the useful contributions of R. Chen towards the derivation of PPE and S-PPE schemes. We acknowledge insightful discussions with F. Becca, D. Poletti, G. Carleo, F. Ferrari and F. Minganti. We thank F. Caleca, M. Schmitt, and J. Dziarmaga for sharing their data with us. We are grateful to L. L. Viteritti, C. Giuliani, A. Kahn, A. Shokry, L. Fioroni, and A. Sinibaldi for assisting in our fight against non-converging simulations, Jax bugs and complicated equations. F.V. acknowledges support by the French Agence Nationale de la Recherche through the NDQM project, grant ANR-23-CE30-0018. V.S. acknowledges support by the Swiss National Science Foundation through Projects No. 200020_185015, 200020_215172, and support from the EPFL Science Seed Fund 2021. This project was provided with computing HPC and storage resources by GENCI at IDRIS thanks to the grant 2023-AD010514908 on the supercomputer Jean Zay’s V100/A100 partition.

During the redaction of this manuscript we were made aware of a late revision of Ref. [53] applying the LPE scheme to fermionic dynamics, referring to it as *Taylor Root Expansion*.

Appendix A: Details on LPE and PPE schemes

The two tables below report the coefficients for the first few orders of the LPE and PPE schemes. The details on the derivation can be found in the subsections following the tables.

o	1	2	3	4
a_1	1	$(1-i)/2$	0.6265	$0.0426 - 0.3946i$
a_2		$(1+i)/2$	$0.1867 - 0.4808i$	$0.0426 + 0.3946i$
a_3			$0.1867 + 0.4808i$	$0.4573 - 0.2351i$
a_4				$0.4573 + 0.2351i$

TABLE IV. Coefficients for the LPE schemes of lowest order. The sets of coefficients presented for each order are not unique: all $s!$ permutations are also solutions. Irrational numbers are reported with a precision of four decimal points. We remark that the first order scheme with a single timestep is equivalent to a standard Euler scheme.

o	2	4	6
a_1	1/2	$(3 - \sqrt{3}i)/12$	0.2153
a_2		$(3 + \sqrt{3}i)/12$	$0.1423 - 0.1358i$
a_3			$0.1423 + 0.1358i$
b_1	-1/2	$(-3 - \sqrt{3}i)/12$	-0.2153
b_2		$(-3 + \sqrt{3}i)/12$	$-0.1423 - 0.1358i$
b_3			$-0.1423 + 0.1358i$

TABLE V. Coefficients for the PPE schemes of lowest order. The sets of coefficients presented for each order are not unique. All the permutations of the a_{js} and of b_{js} are also solutions leading to a total of $[(s/2)!]^2$ combinations. We remark that the second order scheme with a single substep corresponds to a simple midpoint scheme.

The two tables below report the coefficients for the first few orders of the S-LPE and S-PPE schemes.

o	1	2	3
a_1	1	$(1-i)/2$	$0.1057 - 0.3943i$
a_2		$(1+i)/2$	$0.3943 + 0.1057i$
a_3			$0.3943 - 0.1057i$
a_4			$0.1057 + 0.3943i$
α_1	1	$(1-i)/2$	$0.1057 - 0.3943i$
α_2		$(1+i)/2$	$0.3943 + 0.1057i$
α_3			$0.3943 - 0.1057i$
α_4			$0.1057 + 0.3943i$

TABLE VI. Coefficients for the S-LPE schemes of lowest order. We remark that $a_i = \alpha_i$. The sets of coefficients presented for each order are unique up to conjugation. The first order scheme with a single timestep is equivalent to the first order Baker–Campbell–Hausdorff expansion. For S-LPE schemes the coefficient β in Eq. (8) is always vanishing.

o	2	3	4
a_1	1/2	$(3 + \sqrt{3}i)/12$	$(3 - \sqrt{15}i)/24$
a_2		$(3 - \sqrt{3}i)/12$	1/4
a_3			$(3 + \sqrt{15}i)/24$
b_1	-1/2	$(-3 - \sqrt{3}i)/12$	$(-3 + i\sqrt{15})/24$
b_2		$(-3 + \sqrt{3}i)/12$	-1/4
b_3			$(-3 - i\sqrt{15})/24$
α_1	1/2	$(3 + \sqrt{3}i)/12$	$(3 - \sqrt{15}i)/24$
α_2	1/2	1/2	$(9 - \sqrt{15}i)/24$
α_3		$(3 - \sqrt{3}i)/12$	$(9 + \sqrt{15}i)/24$
α_4			$(3 + \sqrt{15}i)/24$

TABLE VII. Coefficients for the S-PPE schemes of lowest order. The sets of coefficients presented for each order are unique up to conjugation. We note that $\alpha_s = 0$ is always followed by $\alpha_{s+1} \neq 0$. This corresponds to a final diagonal operation after the sequence of optimizations.

1. Linear Product Expansion (LPE)

Consider the ordinary differential equation of the form in Eq. (1), where the solution $|\psi(t)\rangle$ is discretized over a set of times $\{t_n\}_{n=1,2,\dots}$, such that $|\psi_n\rangle = |\psi(t_n)\rangle$ and $t_{n+1} - t_n = dt$. The LPE scheme introduced in Section IID provides the following prescription for approximately updating $|\psi_n\rangle$:

$$|\psi_{n+1}\rangle = \left(\prod_{j=1}^s \hat{T}_{a_j} \right) |\psi_n\rangle = |\psi_n\rangle + dt \sum_{j=1}^s a_j |\kappa_j\rangle \quad (\text{A1})$$

where

$$|\kappa_j\rangle = \hat{\Lambda} \left(|\psi_n\rangle + dt \sum_{\ell=1}^{j-1} a_\ell |\kappa_\ell\rangle \right). \quad (\text{A2})$$

This expression is in direct correspondence with the evolution equations of an explicit Runge–Kutta method with update function $f(|\psi\rangle) = \hat{\Lambda}|\psi\rangle$. Although the LPE scheme can be cast as an explicit Runge–Kutta approximation, its scalability relies on avoiding this direct interpretation. Instead, Eq. (A1) is treated as a recursive process defined by

$$|\phi_k\rangle \quad \text{s.t.} \quad |\phi_k\rangle = \hat{T}_{a_k} |\phi_{k-1}\rangle \quad (k = 1, \dots, s) \quad (\text{A3})$$

where $|\psi_{n+1}\rangle \equiv |\phi_s\rangle$, and $|\psi_n\rangle \equiv |\phi_0\rangle$. This is analogous to the formulation given in Eq. (4) in terms of transformations of the variational parameters of the wave function. As explained in the main text, each sub-problem in Eq. (A3) involves at most linear powers of $\hat{\Lambda}$ making its application to NQS far more practical than a direct implementation of the Taylor expansion. The numerical values of the coefficients (a_1, \dots, a_s) are obtained by Taylor expanding both sides of Eq. (6) and matching the terms order by order. This leads to the following linear system of equations for the coefficients:

$$e_k(a_1, \dots, a_s) = \frac{1}{k!} \quad (\text{A4})$$

for $1 \leq k \leq s$. Here, $e_k(a_1, \dots, a_s)$ is the elementary symmetric polynomial of degree k in s variables, defined for $k \leq s$ as the sum of the products of all possible combinations of k distinct elements chosen from the set $\{a_j\}_{j=1}^s$ [111]. We solve these equations in Mathematica for $s \leq 4$ and report the solutions in Table IV. Interestingly, all coefficients a_j for which $\text{Im}\{a_j\} \neq 0$ appear in complex conjugate pairs and $\text{Re}\{a_j\} > 0 \forall j$.

2. Padé Product Expansion (PPE)

The PPE scheme introduced in Section II E provides the following prescription for approximately updating $|\psi_n\rangle$:

$$|\psi_{n+1}\rangle = \left(\prod_{j=1}^s \hat{P}_{b_j, a_j} \right) |\psi_n\rangle = \left(\prod_{j=1}^s \hat{T}_{b_j}^{-1} T_{a_j} \right) |\psi_n\rangle. \quad (\text{A5})$$

While a correspondence with explicit Runge–Kutta methods could be established via the Neumann series expansion of each $\hat{T}_{b_j}^{-1}$ term, the scalability of the method relies on avoiding this expansion. Instead, Eq. (A5) is treated as a recursive problem defined by

$$|\phi_k\rangle \quad \text{s.t.} \quad \hat{T}_{b_k} |\phi_k\rangle = \hat{T}_{a_k} |\phi_{k-1}\rangle \quad (k = 1, \dots, s), \quad (\text{A6})$$

and where $|\psi_{n+1}\rangle \equiv |\phi_s\rangle$, and $|\psi_n\rangle \equiv |\phi_0\rangle$. This recursion relation can be alternatively stated as

$$|\phi_k\rangle = |\psi_n\rangle + dt \sum_{j=1}^k b_j (-\hat{\Lambda}) |\phi_j\rangle + dt \sum_{j=1}^k a_j \hat{\Lambda} |\phi_{j-1}\rangle \quad (k = 1, \dots, s), \quad (\text{A7})$$

which puts the method in direct correspondence with the evolution equations of an implicit-explicit (IMEX) Runge–Kutta method with implicit and explicit update function $g(|\psi\rangle) = -\hat{\Lambda}|\psi\rangle$ and $f(|\psi\rangle) = \hat{\Lambda}|\psi\rangle$ respectively [112, 113].

As for the LPE scheme, the superiority in scalability of the method relies on avoiding this expansion and casting instead the expression onto the nested series of optimizations in Eq. (4). The numerical values of the coefficients $(a_1, \dots, a_s, b_1, \dots, b_s)$ are obtained by Taylor expanding both sides of Eq. (7) and matching the terms order by order. This leads to the following linear system of equations for the coefficients:

$$\sum_{j=0}^k (-1)^{k-j} e_j(a_1, \dots, a_s) h_{k-j}(b_1, \dots, b_s) = 1/k! \quad (\text{A8})$$

for $1 \leq k \leq 2s$. Here, $h_{k-j}(b_1, \dots, b_s)$ is the complete homogeneous symmetric polynomial of degree k in s variables, defined as the sum of all monomials of degree k that can be formed from the set $\{b_j\}_{j=1}^s$ allowing repetition of variables [111]. We adopt the convention that $e_0(a_1, \dots, a_s) = h_0(b_1, \dots, b_s) = 1$, and $e_{j>s}(a_1, \dots, a_s) = 0$. The values of $\{a_j, b_j\}_{j=1}^s$ for $s \leq 3$ satisfying Eq. (A8) are provided in Table V. Interestingly, we note that $a_j = -b_j^*$ and that $\text{Re}\{a_j\} > 0$, $\text{Re}\{b_j\} < 0 \forall j$. As before, if a_j or b_j have nonvanishing imaginary part they appear in conjugate pairs.

a. *Unitarity of Padè Product Expansions*

We here show that PPE schemes are exactly (to all orders in dt) unitary. The fundamental building blocks of PPEs are of the form

$$U_i = P_{b_i, a_i} = \hat{T}_{b_i}^{-1} \hat{T}_{a_i} = \left(\mathbb{1} + b_i \hat{\Lambda} \right)^{-1} \left(\mathbb{1} + a_i \hat{\Lambda} \right), \quad (\text{A9})$$

where the timestep dt has been absorbed into $\hat{\Lambda} = -i\hat{H}dt$. Since \hat{H} is Hermitian, $\hat{\Lambda} = -\hat{\Lambda}^\dagger$ is anti-Hermitian. It follows that

$$\begin{aligned} U_i^\dagger U_i &= \left(\mathbb{1} - a_i^* \hat{\Lambda} \right) \left(\mathbb{1} - b_i^* \hat{\Lambda} \right)^{-1} \left(\mathbb{1} + b_i \hat{\Lambda} \right)^{-1} \left(\mathbb{1} + a_i \hat{\Lambda} \right) \\ &= \left(\mathbb{1} - a_i^* \hat{\Lambda} \right) \left(\mathbb{1} + b_i \hat{\Lambda} \right)^{-1} \left(\mathbb{1} - b_i^* \hat{\Lambda} \right)^{-1} \left(\mathbb{1} + a_i \hat{\Lambda} \right), \end{aligned} \quad (\text{A10})$$

where in the last equality we used that $[(\mathbb{1} + a\hat{A})^{-1}, \mathbb{1} + \hat{A}] = 0$: a trivial consequence of the fact that $[\hat{A}, f(\hat{A})] = 0$ for any $\hat{A} \in \mathcal{H}$ and $f : \mathcal{H} \rightarrow \mathcal{H}$. From Table V we observe that the expansion coefficients are related by $a_i = -b_i^*$. Substituting this in Eq. (A10) leads to

$$U_i^\dagger U_i = \left(\mathbb{1} + b_i \hat{\Lambda} \right) \left(\mathbb{1} + b_i \hat{\Lambda} \right)^{-1} \left(\mathbb{1} + a_i \hat{\Lambda} \right)^{-1} \left(\mathbb{1} + a_i \hat{\Lambda} \right) = \mathbb{1}. \quad (\text{A11})$$

PPE expansions of arbitrary order $o = 2s$ obtained as $\hat{U} = \prod_{i=1}^s U_i$ are therefore unitary, that is $\hat{U}^\dagger \hat{U} = \mathbb{1}$. To be precise, the relation $a_i = -b_i^*$ holds only for a subset of all possible solutions to Eq. (A8). In general, however, the relation $a_i = -\text{Re}\{b_i\} \pm \text{Im}\{b_i\}$ holds. Moreover, the b_i s always present in conjugate pairs so that the proof can be carried out analogously.

Analogous calculations can be applied to the S-PPE-2 scheme. Here, since all coefficients are real, the diagonal terms in $\hat{U}^\dagger \hat{U}$ cancel out, making the algorithm exactly unitary. This does not hold for S-PPE schemes of higher order for which the α_i s are in general complex.

Appendix B: Control variates for the conditional Monte-Carlo estimator [Eq. (22)]

Control variates are particularly effective when both the control variable and its coefficient can be derived analytically. For the simple Monte Carlo estimator of the fidelity in Eq. (19) of the main text, this is done in Ref. [47], where the identity $\mathbb{E}_{(x,y) \sim \pi} [|A(x,y)|^2] = 1$ is directly employed to reduce the variance of the estimator leading to Eq. (21). To identify an analogous control variable for the cmc estimator we can proceed in one of two ways. The first approach recognizes that the cmc estimator arises from conditioning the smc estimator, and therefore the control-variate-enhanced cmc estimator naturally follows from conditioning the cv-smc estimator. Specifically we have that

$$\mathcal{F}(|\psi\rangle, |\phi\rangle) = \mathbb{E}_{(x,y) \sim \pi} [F(x,y)] = \mathbb{E}_{x \sim \pi_\psi} [\mathbb{E}_{y \sim \pi_\phi} [F(x,y)|x]], \quad (\text{B1})$$

corresponds exactly to Eq. (23). The second approach observes that $|A(z)|^2$ is correlated with $H_{\text{loc}}(x)$ and thus remains a valid control variable for the cmc estimator. By leveraging the separability of both $\pi(x,y) = \pi_\psi(x)\pi_\phi(y)$, and $A(x,y) = A_x(x)A_y(y)$, $(|A(x,y)|^2 - 1)$ we can apply control variates to the cmc estimator as follows

$$\begin{aligned} \mathcal{F}(|\psi\rangle, |\phi\rangle) &= \mathbb{E}_{x \sim \pi_\psi} \left[\text{Re}\{H_{\text{loc}}\} + c \left(\mathbb{E}_{(x,y) \sim \pi} |A(x,y)|^2 - 1 \right) \right], \\ &= \mathbb{E}_{x \sim \pi_\psi} \left[\text{Re}\{H_{\text{loc}}\} + c \left(|A_x(x)|^2 \mathbb{E}_{y \sim \pi_\phi} [|A_y(y)|^2] - 1 \right) \right], \end{aligned} \quad (\text{B2})$$

which again corresponds to Eq. (23). Here, $A_x(x) = \phi(x)/\psi(x)$, and $A_y(y) = \psi(y)/\phi(y)$. With a derivation similar to that in Ref. [47], we find that the optimal control coefficient c , which minimizes the variance of the cv-cmc estimator, converges to $c = -1/2$ as $|\psi\rangle \rightarrow |\phi\rangle$.

In Fig. 8 we illustrate the variance reduction achieved by applying control variates to the smc and cmc estimators. The data clearly highlight the efficiency of control variates in reducing the variance for both estimators. These calculations were performed in a regime far from ideal convergence, resulting in slight deviations from the expected optimal value of $c = -1/2$. In accordance with the Rao-Blackwell theorem, the variance of the cv-cmc estimator is consistently lower than that of the cv-smc estimator for any choice of c .

We further note that in both control-variate-enhanced expressions, we retain only the real part of the original estimator because the fidelity is known to be real, ensuring that $\mathbb{E}_\chi[\text{Im}\{f\}] = 0$ for $f = A, H_{\text{loc}}$. Including the imaginary part would introduce an additional control variable with zero mean. However, as $\text{Im}\{f\}$ is uncorrelated with $\text{Re}\{f\}$, this additional control variable does not contribute any variance reduction and is therefore discarded.

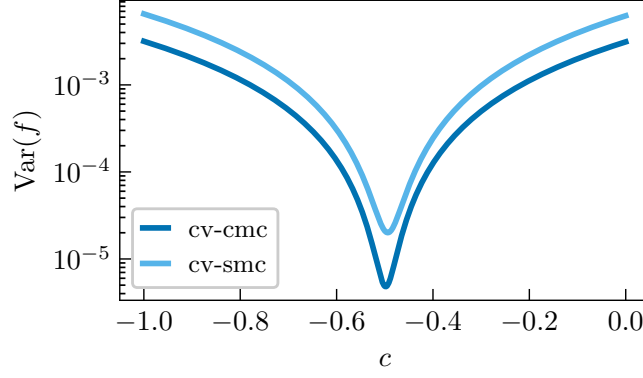


FIG. 8. Variance comparison of controlled estimators Eq. (21) (cv-smc) and Eq. (23) (cv-cmc) as a function of the control coefficient c .

Appendix C: Derivation of the gradient estimators

In this section we derive and discuss the properties of different possible Monte Carlo estimators for the gradient of the fidelity. To do in an efficient manner we introduce the notation

$$z = (x, y), \quad \pi_\psi(x) = \frac{|\psi(x)|^2}{\langle \psi | \psi \rangle}, \quad \pi(z) = \pi_\psi(x)\pi_\phi(y), \quad A(z) = \frac{\phi(x)\psi(y)}{\phi(y)\psi(x)}. \quad (\text{C1})$$

In the following we consider a complex ansatz $[\psi_\theta(x) \in \mathbb{C}]$ and real parameters $(\theta \in \mathbb{R}^{N_p})$. As we have done throughout the paper, we identify the variational state as $\psi = \psi_\theta$, making implicit the dependence of the variational state $|\psi\rangle$ on the variational parameters.

1. Derivation of the ∇ cmc gradient estimator [Eq. (26)]

We derive the ∇ cmc estimator of the gradient in Eq. (26) by differentiating the cmc fidelity estimator $\mathcal{F} = \mathbb{E}_{x \sim \pi_\psi}[H_{\text{loc}}(x)]$ in Eq. (22). We show that this gradient estimator can admit the form $\nabla \mathcal{F} = \mathbf{X}\varepsilon$ for suitable choices of \mathbf{X} and ε .

Applying the chain rule to \mathcal{F} yields two contributions to the gradient

$$\nabla \mathcal{F} = \nabla \sum_x \pi_\psi(x) H_{\text{loc}}(x) = \underbrace{\sum_x H_{\text{loc}}(x) \nabla \pi_\psi(x)}_{\textcircled{1}} + \underbrace{\sum_x \pi_\psi(x) \nabla H_{\text{loc}}(x)}_{\textcircled{2}}. \quad (\text{C2})$$

First off, we have that

$$\nabla \pi_\psi(x) = \nabla \frac{\langle \psi | x \rangle \langle x | \psi \rangle}{\langle \psi | \psi \rangle} = \frac{\langle \nabla \psi | x \rangle \langle x | \psi \rangle + \langle \psi | x \rangle \langle x | \nabla \psi \rangle}{\langle \psi | \psi \rangle} - \frac{\langle \psi | x \rangle \langle x | \psi \rangle \langle \nabla \psi | \psi \rangle + \langle \psi | \nabla \psi \rangle}{\langle \psi | \psi \rangle} = 2\pi_\psi(x) \Delta J^{\text{re}}(x), \quad (\text{C3})$$

where we denote $A^{\text{re}} \equiv \text{Re}\{A\}$ and $A^{\text{im}} \equiv \text{Im}\{A\}$. It follows that

$$\textcircled{1} = \sum_x H_{\text{loc}}(x) \nabla \pi_\psi(x) = \mathbb{E}_{x \sim \pi_\psi}[2\Delta J^{\text{re}}(x) H_{\text{loc}}(x)]. \quad (\text{C4})$$

Then we use that $H_{\text{loc}}(x) = \langle x | \hat{H} | \psi \rangle / \langle x | \psi \rangle$ with $\hat{H} = |\phi\rangle\langle\phi| / \langle\phi|\phi\rangle$ to compute

$$\nabla H_{\text{loc}}(x) = \nabla \frac{\langle x | \hat{H} | \psi \rangle}{\langle x | \psi \rangle} = \frac{\langle x | \hat{H} | \nabla \psi \rangle}{\langle x | \psi \rangle} - H_{\text{loc}}(x) \frac{\langle x | \nabla \psi \rangle}{\langle x | \psi \rangle} = \frac{\langle x | \hat{H} | \nabla \psi \rangle}{\langle x | \psi \rangle} - H_{\text{loc}}(x) J(x) \quad (\text{C5})$$

so that,

$$\textcircled{2} = \sum_x \pi_\psi(x) \nabla H_{\text{loc}}(x) = -2i \mathbb{E}_{x \sim \pi_\psi} [J(x) H_{\text{loc}}^{\text{im}}(x)]. \quad (\text{C6})$$

Since \hat{H} is Hermitian, we know that $\langle \psi | \hat{H} | \psi \rangle = \mathbb{E}_{x \sim \pi_\psi} [H_{\text{loc}}(x)] \in \mathbb{R}$ and therefore that $\mathbb{E}_{x \sim \pi_\psi} [H_{\text{loc}}^{\text{im}}(x)] = 0$. We can thus use that $H_{\text{loc}}^{\text{im}} = \Delta H_{\text{loc}}^{\text{im}}$ to obtain

$$\textcircled{2} = -2i \mathbb{E}_{x \sim \pi_\psi} [J(x) \Delta H_{\text{loc}}^{\text{im}}(x)] = -2i \mathbb{E}_{x \sim \pi_\psi} [\Delta J(x) H_{\text{loc}}^{\text{im}}(x)]. \quad (\text{C7})$$

Finally,

$$\begin{aligned} \nabla \mathcal{F} &= \textcircled{1} + \textcircled{2} = \mathbb{E}_{x \sim \pi_\psi} [2\Delta J^{\text{re}}(x) H_{\text{loc}}(x) - 2i \Delta J(x) H_{\text{loc}}^{\text{im}}(x)] \\ &= \mathbb{E}_{x \sim \pi_\psi} [2 \text{Re}\{\Delta J(x) H_{\text{loc}}(x)^*\}] = 2 \mathbb{E}_{x \sim \pi_\psi} [\Delta J_x^{\text{re}} H_{\text{loc}}^{\text{re}}(x) + \Delta J_x^{\text{im}} H_{\text{loc}}^{\text{im}}(x)] \\ &= \mathbb{E}_{x \sim \pi_\psi} \left[\begin{pmatrix} \Delta J^{\text{re}}(x) \\ \Delta J^{\text{im}}(x) \end{pmatrix} \cdot \begin{pmatrix} 2 \text{Re}\{H_{\text{loc}}(x)\} \\ 2 \text{Im}\{H_{\text{loc}}(x)\} \end{pmatrix} \right] = \text{Cov}_{x \sim \pi_\psi} \left[\begin{pmatrix} J^{\text{re}}(x) \\ J^{\text{im}}(x) \end{pmatrix}, \begin{pmatrix} 2 \text{Re}\{H_{\text{loc}}(x)\} \\ 2 \text{Im}\{H_{\text{loc}}(x)\} \end{pmatrix} \right]. \end{aligned} \quad (\text{C8})$$

We can now explicit the Monte-Carlo sampling of the expectation value which is in practice evaluated as

$$\nabla \mathcal{F} \approx \frac{2}{N_s} \sum_{i=1}^{N_s} \Delta J^{\text{re}}(x_i) H_{\text{loc}}^{\text{re}}(x_i) + \Delta J^{\text{im}}(x_i) H_{\text{loc}}^{\text{im}}(x_i) = \frac{2}{N_s^2} \sum_{i,j=1}^{N_s} \Delta J^{\text{re}}(x_i) A^{\text{re}}(x_i, y_j) + \Delta J^{\text{im}}(x_i) A^{\text{im}}(x_i, y_j), \quad (\text{C9})$$

with N_s the number of samples. Note that the second expression follows from the fact that the local estimator itself is evaluated with MC sampling as

$$H_{\text{loc}}(x) = \frac{\phi(x)}{\psi(x)} \frac{1}{N_s} \sum_{j=1}^{N_s} \frac{\psi(y_j)}{\phi(y_j)}. \quad (\text{C10})$$

We now want to express the above in a form compatible with NTK and automatic damping strategies. To account for the fact that we want to work with real quantities, we modify slightly the definition of \mathbf{X} gave in the main text. Specifically, we take \mathbf{Y} to be defined as in Eq. (14), that is,

$$\mathbf{Y} = \frac{1}{\sqrt{N_s}} [\Delta J(x_1)^\dagger | \dots | \Delta J(x_{N_s})^\dagger] \in \mathbb{C}^{N_p \times N_s}. \quad (\text{C11})$$

and define \mathbf{X} as the concatenation of its real and imaginary parts as

$$\mathbf{X} = \text{Concat}[\text{Re}\{\mathbf{Y}\}, \text{Im}\{\mathbf{Y}\}] = \begin{pmatrix} \text{Re}\{\mathbf{Y}\} \\ \text{Im}\{\mathbf{Y}\} \end{pmatrix} \in \mathbb{R}^{N_p \times 2N_s}. \quad (\text{C12})$$

In this way, the QGT is $\mathbf{S} = \mathbf{X} \mathbf{X}^T$, the NTK $\mathbf{T} = \mathbf{X}^T \mathbf{X}$. We then define the complex local energy as

$$f = \frac{2}{\sqrt{N_s}} (H_{\text{loc}}(x_1), \dots, H_{\text{loc}}(x_{N_s})) \in \mathbb{C}^{N_s} \quad (\text{C13})$$

and its real counterpart as $\varepsilon = \text{Concat}[\text{Re}\{f\}, \text{Im}\{f\}] \in \mathbb{R}^{2N_s}$. It is easy to see that we can express Eq. (C9) as $\nabla \mathcal{F} = \mathbf{X} \varepsilon$.

2. Derivation of the $\nabla \text{cv-smc}$ gradient estimator [Eq. (27)]

We derive the $\nabla \text{cv-smc}$ estimator of the gradient in Eq. (27) by differentiating the cv-smc fidelity estimator $\mathcal{F} = \mathbb{E}_{z \sim \pi} [F(z)] = \mathbb{E}_{z \sim \pi} [\text{Re} A(z) + c(|A(z)|^2 - 1)]$ in Eq. (21). We show that this gradient estimator does not admit the form $\nabla \mathcal{F} = \mathbf{X} \varepsilon$ and is therefore unsuited for NTK calculations.

Once again

$$\nabla \mathcal{F} = \nabla \sum_z \pi(z) F(z) = \underbrace{\sum_z F(z) \nabla \pi(z)}_{\textcircled{1}} + \underbrace{\sum_z \pi(z) \nabla F(z)}_{\textcircled{2}}. \quad (\text{C14})$$

Since $\nabla\pi = \pi_\phi \nabla\pi_\psi$, Eq. (C3) gets us $\textcircled{1} = \mathbb{E}_{z \sim \pi} [2\Delta F(z) J^{\text{re}}(x)]$. Differentiating $A(z)$ yields $\nabla A(z) = A(z)[J(y) - J(x)]$, so that

$$\nabla F(z) = \frac{\nabla A(z) + \nabla A^*(z)}{2} + c \left(A(z) \nabla A^*(z) + A^*(z) \nabla A(z) \right) = \text{Re} \left\{ \left(A(z) + 2c|A(z)|^2 \right) \left(J(y) - J(x) \right) \right\}. \quad (\text{C15})$$

Inserting this into the expression for $\textcircled{2}$ leads to

$$\textcircled{2} = \mathbb{E}_{z \sim \pi} \left[\left(A^{\text{re}}(z) + 2c|A(z)|^2 \right) \left(J^{\text{re}}(y) - J^{\text{re}}(x) \right) + A^{\text{im}}(z) \left(J^{\text{im}}(x) - J^{\text{im}}(y) \right) \right]. \quad (\text{C16})$$

The gradient is then found to be

$$\nabla_\theta \mathcal{F} = \textcircled{1} + \textcircled{2} = \mathbb{E}_{z \sim \pi} \left[\begin{pmatrix} J^{\text{re}}(x) \\ J^{\text{im}}(x) \\ J^{\text{re}}(y) \\ J^{\text{im}}(y) \end{pmatrix} \cdot \begin{pmatrix} 2\Delta F(z) - A^{\text{re}}(z) - 2c|A(z)|^2 \\ A^{\text{im}}(z) \\ A^{\text{re}}(z) + 2c|A(z)|^2 \\ -A^{\text{im}}(z) \end{pmatrix} \right]. \quad (\text{C17})$$

We remark that this estimator evaluates the Jacobian of ψ not only on the samples of ψ as we would normally expect, but on those of ϕ as well. Equation (C17) makes it manifest that this estimator cannot be expressed as $\nabla \mathcal{F} = \mathbf{X} \varepsilon$.

3. Derivation of the ∇ smc gradient estimator [Eq. (25)]

We derive the ∇ smc estimator of the gradient $\mathcal{F} = \mathbb{E}_{(x,y) \sim \pi} [A(x,y)]$ in Eq. (25) and show that it admits the form $\nabla \mathcal{F} = \mathbf{X} \varepsilon$ for suitable choices of \mathbf{X} and ε .

One straightforward approach is to reverse the marginalization yielding the ∇ cmc gradient estimator [Eq. (26)] as

$$\begin{aligned} \nabla_\theta \mathcal{F} &= \mathbb{E}_{x \sim \pi_\psi} [2 \text{Re} \{ \Delta J(x)^* H_{\text{loc}}(x) \}] = 2 \text{Re} \left\{ \sum_x \pi_\psi(x) \Delta J^*(x) H_{\text{loc}}(x) \right\} \\ &= 2 \text{Re} \left\{ \sum_x \pi_\psi(x) \Delta J(x)^* \frac{\phi(x)}{\psi(x)} \sum_y \pi_\phi(y) \frac{\psi(y)}{\phi(x)} \right\} = \mathbb{E}_{z \sim \pi} [2 \text{Re} \{ \Delta J(x) A(z)^* \}] \\ &= \mathbb{E}_{z \sim \pi} \left[\begin{pmatrix} \Delta J^{\text{re}}(x) \\ \Delta J^{\text{im}}(x) \end{pmatrix} \cdot \begin{pmatrix} 2 \text{Re} \{ A(z) \} \\ 2 \text{Im} \{ A(z) \} \end{pmatrix} \right] = \text{Cov}_{z \sim \pi} \left[\begin{pmatrix} J^{\text{re}}(x) \\ J^{\text{im}}(x) \end{pmatrix} \cdot \begin{pmatrix} 2 \text{Re} \{ A(z) \} \\ 2 \text{Im} \{ A(z) \} \end{pmatrix} \right]. \end{aligned} \quad (\text{C18})$$

In practice, the expectation value above is evaluated using MC sampling as

$$\nabla \mathcal{F} \approx \frac{1}{N_s} \sum_{i=1}^{N_s} \Delta J^{\text{re}}(x_i) A(x_i, y_i) + \Delta J^{\text{im}}(x_i) A(x_i, y_i), \quad (\text{C19})$$

which makes manifest the possibility of expressing the gradient as $\nabla \mathcal{F} = \mathbf{X} \varepsilon$ with

$$f = \frac{2}{\sqrt{N_s}} \left(A(x_1, y_1), \dots, A(x_{N_s}, y_{N_s}) \right) \in \mathbb{C}^{N_s} \quad (\text{C20})$$

and $\varepsilon = \text{Concat}[\text{Re}\{f\}, \text{Im}\{f\}] \in \mathbb{R}^{2N_s}$.

Although this derivation would suffice, it is still insightful to explore how the same expression can be obtained by manipulating the ∇ cv-smc estimator [Eq. (27), or equivalently Eq. (C17)]. The value in this alternative derivation stems from the properties of $A(z)$ that this approach reveals. We believe these properties could be useful in the future to derive control variables tailored to the gradient. For starters, we find that

$$\mathbb{E}_{z \sim \pi} [|A(z)|^2 f(x)] = \mathbb{E}_{y \sim \pi_\phi} [f(y)]. \quad (\text{C21})$$

Using this identity, one can easily show that

$$\mathbb{E}_{z \sim \pi} [A^*(z) f(x)] = \mathbb{E}_{z \sim \pi} [A(z) f(y)], \quad (\text{C22})$$

$$\mathbb{E}_{z \sim \pi} [A^*(z) f(y)] = \mathbb{E}_{z \sim \pi} [A(z) f(x)], \quad (\text{C23})$$

$$\mathbb{E}_{z \sim \pi} [A(z) f(x)] = \mathbb{E}_{z \sim \pi} [A^*(z) f(y)], \quad (\text{C24})$$

$$\mathbb{E}_{z \sim \pi} [A(z) f(y)] = \mathbb{E}_{z \sim \pi} [A^*(z) f(x)]. \quad (\text{C25})$$

Again, these equations can be combined to show that

$$\mathbb{E}_{z \sim \pi}[f(x) \operatorname{Re}\{A(z)\}] = \mathbb{E}_{z \sim \pi}[f(y) \operatorname{Re}\{A(z)\}], \quad (\text{C26})$$

$$\mathbb{E}_{z \sim \pi}[f(x) \operatorname{Im}\{A(z)\}] = -\mathbb{E}_{z \sim \pi}[f(y) \operatorname{Im}\{A(z)\}]. \quad (\text{C27})$$

Substitution into Eq. (C17) yields Eq. (C18).

Appendix D: Covariance structure, Rao-Blackwellization, and variance reduction

We use this appendix to expand on the differences in variance exhibited by the gradient estimators presented in the main text. First off, we note that while both the ∇cmc and ∇smc estimators take the form of a covariance estimator [c.f. Eqs. (C8) and (C18)], the $\nabla\text{cv-smc}$ estimator does not. Generally, estimators structured as covariances tend to exhibit lower variance largely due to the inherent variance reduction from centering each component. Specifically, the sample covariance used to estimate the covariance between two random variables X and Y is given by

$$\operatorname{Cov}(X, Y) = \mathbb{E}[(X - \mathbb{E}[X])(Y - \mathbb{E}[Y])] \approx \frac{\gamma}{N_s} \sum_{i=1}^{N_s} \left(X_i - \frac{1}{N_s} \sum_{j=1}^{N_s} X_j \right) \left(Y_i - \frac{1}{N_s} \sum_{j=1}^{N_s} Y_j \right), \quad (\text{D1})$$

where $\gamma = N_s/(N_s - 1)$ is the Bessel correction factor used to remove the bias introduced by centering. The centering process effectively provides sample-specific control variates that automatically adjust to the non-stationarity of the variables, enhancing estimator stability, and justifying the results presented in the main text and further corroborated by Fig. 9.

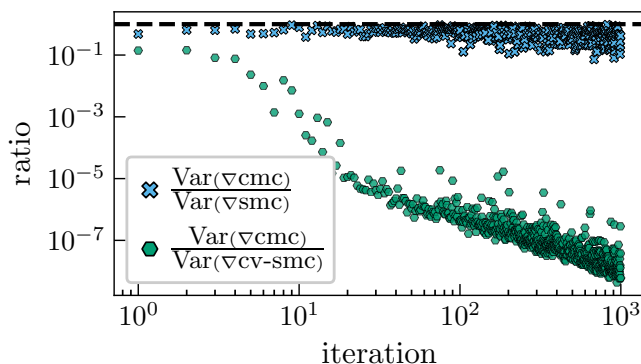


FIG. 9. Comparison of the variance of the different estimators of the fidelity gradient. As the gradient is a vector in \mathbb{R}^{N_p} , for each estimator we consider the component with minimal variance. Statistics are computed on the same data of Fig. 3, specifically on the 300th iterate.

While the poor performance of the $\nabla\text{cv-smc}$ estimator is attributed to its lack of a covariance structure, the smaller performance difference between the ∇cmc and ∇smc estimators can be understood through the Rao-Blackwell theorem. Identical arguments apply for the cmc and smc estimators of the fidelity itself. In the simplest setting, Rao-Blackwellization replaces a function of two random variables with its conditional expectation resulting in a new estimator whose variance is no greater than that of the original function (Rao-Blackwell theorem). Consider two random variables, X and Y , and a function $J(X, Y)$. Our goal is to compute its expectation $\mathbb{E}[J(X, Y)]$ with respect to the joint distribution of X and Y . To do so, we define [95]

$$\mathbb{E}[J(X, Y) | X] = \sum_y J(x, y) \cdot P(Y = y | X = x) \equiv \hat{J}(X) \quad (\text{D2})$$

and note that $\mathbb{E}[\hat{J}(X)] = \mathbb{E}[J(X, Y)]$. This implies that $\hat{J}(X)$ can be used in place of $J(X, Y)$ in a Monte Carlo approximation of $\mathbb{E}[J(X, Y)]$. The variance of $\hat{J}(X)$ can be easily computed to be

$$\operatorname{Var}(\hat{J}(X)) = \operatorname{Var}(J(X, Y)) - \mathbb{E}[(J(X, Y) - \hat{J}(X))^2], \quad (\text{D3})$$

from which it follows that $\text{Var}(\hat{J}(X)) \leq \text{Var}(J(X, Y))$. To compute Rao-Blackwellized estimators, we generally need to calculate conditional expectations. In many cases, this cannot be done exactly; however, under a mean-field assumption, the conditional expectation simplifies due to factorization:

$$\hat{J}(X) = \mathbb{E}[J(X, Y) | X] = \sum_y J(x, y) \cdot P(Y = y | X = x) = \sum_y J(x, y) \cdot P(Y = y) = \mathbb{E}_Y[J(X, Y)], \quad (\text{D4})$$

where we used that $P(X, Y) = P(X)P(Y)$ and thus $P(Y | X) = P(Y)$. Therefore, to construct a lower variance estimator when the joint distribution factorizes, all we need to do is integrate out some variables and use this marginal as the estimator.

Appendix E: Lowering sampling cost by reweighting

Direct evaluation of the fidelity (and of its gradient) between two transformed states $|\tilde{\psi}\rangle = \hat{V}|\psi\rangle$ and $|\tilde{\phi}\rangle = \hat{U}|\phi\rangle$ requires, in principle, sampling from their Born distributions $\pi_{\tilde{\psi}}(x)$ and $\pi_{\tilde{\phi}}(y)$, respectively. This process introduces a computational overhead that scales with N_c , the number of connected elements in the transformations. For local spin Hamiltonians, this introduces a sampling overhead proportional to the system size N , which often becomes the dominant cost (in the simulations presented in Section IV, for instance, around 90% of the computational time is spent sampling). The computational burden grows substantially for other Hamiltonians, such as for those arising in natural-orbital chemistry or for the kinetic term in first-quantisation formulations [114].

To address this overhead, one can resort to self-normalizing importance sampling [94], adapting the estimators discussed in Sections III and III C 2 to sample directly from the bare distributions. While this reduces the sampling complexity, it's important to note that this modification may increase the variance and introduce bias in the estimator, requiring careful benchmarking to ensure its effectiveness. In line with the procedure outlined in Ref. [47], we avoid direct sampling from the target state. While previous works were concerned with unitary transformations applied to the target state alone, here we extend the approach to arbitrary transformations that act on both the target and variational states.

As all estimators discussed in Sections III and III C 2 are of this form, it is convenient to write down the self-normalizing reweighting procedure just once for the generic estimator $\mathbb{E}_{\sigma \sim \chi}[f(\sigma)]$. In this case, we have [94]

$$\mathbb{E}_{\sigma \sim \chi}[f(\sigma)] = \frac{\mathbb{E}_{\sigma \sim \eta}[w(\sigma)f(\sigma)]}{\mathbb{E}_{\sigma \sim \eta}[w(\sigma)]}, \quad (\text{E1})$$

where $w = \eta/\chi$. Specializing to the case where we sample from a joint distribution, e.g. in Eqs. (19), (21), (25) and (27), yields

$$\mathbb{E}_{(x,y) \sim \tilde{\pi}}[f(x, y)] = \frac{\sum_{x,y} \pi(x, y) \frac{\tilde{\pi}(x,y)}{\pi(x,y)} f(x, y)}{\sum_{x,y} \pi(x, y) \frac{\tilde{\pi}(x,y)}{\pi(x,y)}}, \quad (\text{E2})$$

where $\tilde{\pi}(x, y) = \pi_{\tilde{\psi}}(x)\pi_{\tilde{\phi}}(y)$. We can use the above, the separability of the distribution, and the separability of the integrator $f(x, y) = f_x(x)f_y(y)$ that we have in the remaining cases of Eqs. (22), (23) and (26) to get

$$\mathbb{E}_{(x,y) \sim \tilde{\pi}}[f(x, y)] = \mathbb{E}_{x \sim \tilde{\pi}_\psi}[f_x(x)]\mathbb{E}_{y \sim \tilde{\pi}_\phi}[f_y(y)] = \frac{\sum_x \pi_\psi(x) \frac{\tilde{\pi}_\psi(x)}{\pi_\psi(x)} f_x(x)}{\sum_x \pi_\psi(x) \frac{\tilde{\pi}_\psi(x)}{\pi_\psi(x)}} \frac{\sum_y \pi_\phi(y) \frac{\tilde{\pi}_\phi(y)}{\pi_\phi(y)} f_y(y)}{\sum_y \pi_\phi(y) \frac{\tilde{\pi}_\phi(y)}{\pi_\phi(y)}}. \quad (\text{E3})$$

While these estimators are much cheaper to compute, as anticipated above, they may perform more poorly than their original counterparts. As an example we can take the generic covariance estimator which is reweighted as

$$\text{Cov}_{\sigma \sim \chi}(f, g) = \mathbb{E}_\chi[(f - \mathbb{E}_\chi[f])(g - \mathbb{E}_\chi[g])] = \mathbb{E}_\chi[fg] - \mathbb{E}_\chi[f] \mathbb{E}_\chi[g] \quad (\text{E4})$$

$$= \mathbb{E}_{\sigma \sim \eta} \left[\frac{w(\sigma)}{N_\chi} f(\sigma)g(\sigma) \right] - \mathbb{E}_{\sigma \sim \eta} \left[\frac{w(\sigma)}{N_\chi} f(\sigma) \right] \mathbb{E}_{\sigma \sim \eta} \left[\frac{w(\sigma)}{N_\chi} g(\sigma) \right], \quad (\text{E5})$$

with $N_\chi = \mathbb{E}_{\sigma \sim \eta}[w(\sigma)]$. The reweighted estimator no longer exhibits the covariance structure identified in Appendix D as being associated with good variance performance.

Appendix F: Machine precision on small systems and the limitation of Monte Carlo sampling

We now demonstrate the theoretical possibility of solving infidelity optimizations to machine precision. Specifically, we revisit the same quench dynamics studied in Section IV B from $h = \infty$ to $h = h_c/10$, but on a smaller 4×4 lattice where expectation values can be computed exactly in full summation.

In Fig. 10(a-b) we compare the variational dynamics carried out in full-summation against exact simulations. The results show perfect agreement with the exact solution, with optimizations converging to the target state with machine precision.

However, Monte Carlo simulations of the same dynamics exhibit results comparable to those shown in Section IV A, where convergence is good but falls short of machine precision. As discussed in Section III C 4, this discrepancy is likely due to the poor estimation of the curvature matrix when using a limited number of samples, leading to unreliable updates. Indeed, increasing the number of samples significantly improves the results, as convergence towards the full summation results is approached. Unfortunately, solutions compatible with the ones in full summation seem to require a sample size on the order of the size of the entire Hilbert space.

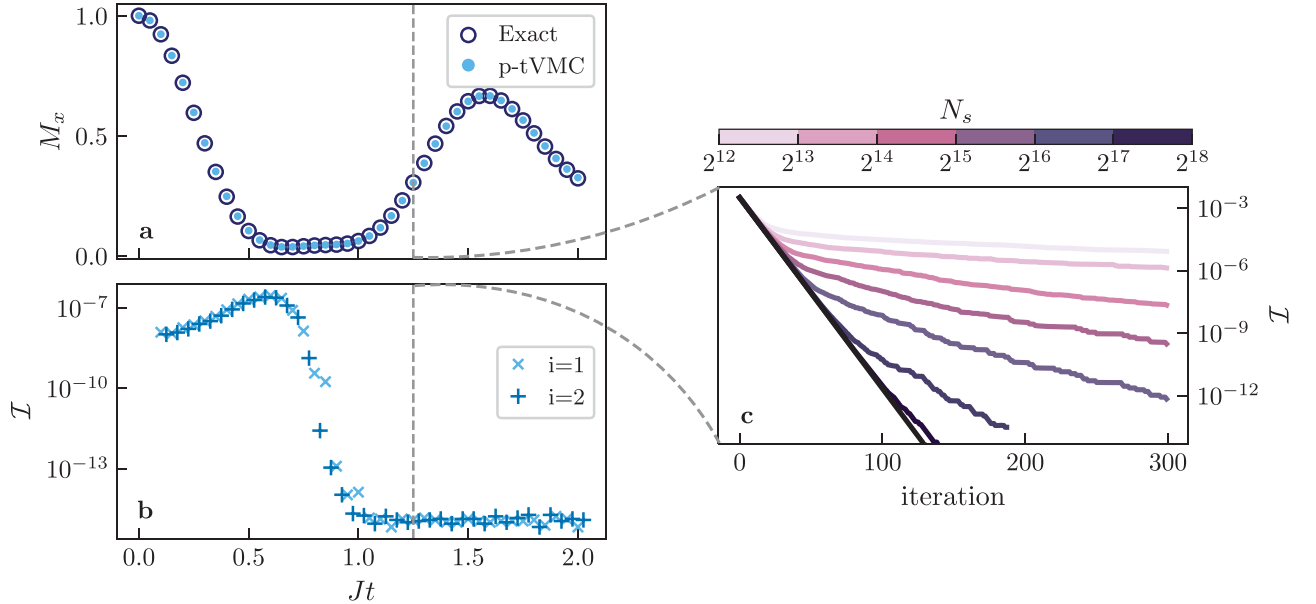


FIG. 10. Quenched dynamics ($h = \infty \rightarrow h_c/10$) on a 4×4 lattice. (a,b) Average magnetization and optimization infidelity as a function of time. The variational results (full dots) are obtained in full summation using the S-LPE-2 scheme with $dt = 0.05$. We compare this to the exact calculation (open circles). We remark that convergence within numerical precision in the optimizations for $Jt \gtrsim 1$. (c) Optimization profiles for the update $Jt = 1.25 \rightarrow 1.30$ for different sample sizes N_s . The convergence is negatively impacted by the lack a number of samples sufficient to properly reconstruct the QGT. Stochastic optimization achieve performance compatible with full summation (black line) only for very large sample sizes, comparable or superior to the size of the Hilbert space. Each optimization is initialized in the state obtained in full summation for $Jt = 1.25$. We use a fixed learning rate $\alpha = 0.05$ and a complex CNN with $\Theta_{\text{CNN}} = (10, 10, 10, 10; 3)$ for all simulations. The regularization coefficient λ is fixed to $\lambda = 10^{-8}$ for $N_s = \infty, 2^{18}, 2^{17}, 2^{16}$. Smaller sample sizes require stronger regularization. We use $\lambda = 10^{-7}$ for $N_s = 2^{15}, 2^{14}$ and $\lambda = 10^{-6}$ for $N_s = 2^{13}, 2^{12}$.

Appendix G: Exact application of diagonal operators

Let $|\psi_\theta\rangle = \sum_x \psi_\theta(x) |x\rangle$ be a variational state and $\hat{A} = \sum_{x,y} A_{xy} |x\rangle\langle y|$ a generic operator acting on it. We want to find a way to reduce the application of \hat{A} on $|\psi_\theta\rangle$ to a change of parameters $\theta \rightarrow \theta'$. In other words, we want to find θ' such that

$$|\psi_{\theta'}\rangle = \hat{A} |\psi_\theta\rangle. \quad (\text{G1})$$

If successful, this procedure would allow us to apply \hat{A} on $|\psi_\theta\rangle$ exactly and at no computational expense. Unfortunately, for a generic parametrization of the state, or a generic operator, this is not possible. The problem greatly simplifies

if we restrict to diagonal operators of the form $\hat{A} = \sum_x A_x |x\rangle\langle x|$, whose application on a generic variational state reads $\hat{A}|\psi_\theta\rangle = \sum_x A_x \psi_\theta(x) |x\rangle$. Even in this simple case, the transformation $\theta \rightarrow \theta'$ satisfying $|\psi_{\theta'}\rangle = \hat{A}|\psi_\theta\rangle$ is not guaranteed to exist. Consider, however, the improved ansatz $|\psi_{\theta,\phi}\rangle = \sum_x \psi_{\theta,\phi}(x) |x\rangle$ where

$$\psi_{\theta,\phi}(x) = (A_x)^\phi \psi_\theta(x) \quad \text{with} \quad \phi \in \mathbb{C}. \quad (\text{G2})$$

The application of \hat{A} on this state reads

$$\hat{A}|\psi_{\theta,\phi}\rangle = \sum_x A_x \psi_{\theta,\phi}(x) |x\rangle = \sum_x (A_x)^{\phi+1} \psi_\theta(x) |x\rangle = |\psi_{\theta,\phi+1}\rangle \quad (\text{G3})$$

The action of \hat{A} on $|\psi_{\theta,\phi}\rangle$ can thus be *exactly* reduced to the parameter transformation $(\theta, \phi) \rightarrow (\theta, \phi + 1)$ which can be computed at virtually no computational expense. Note that while the additional multiplicative layer has a structure determined by \hat{A} , the network $\psi_\theta(x)$ to which this layer is added is completely arbitrary.

This procedure can be easily generalized to multiple diagonal operations which, of course, commute with each other. Given $\hat{A} = \sum_x A_x |x\rangle\langle x|$ and $\hat{B} = \sum_x B_x |x\rangle\langle x|$, we define the improved ansatz as

$$\psi_{\theta,\phi_A,\phi_B}(x) = (B_x)^{\phi_B} (A_x)^{\phi_A} \psi_\theta(x). \quad (\text{G4})$$

The application of \hat{A} without \hat{B} is equivalent to $(\theta, \phi_A, \phi_B) \rightarrow (\theta, \phi_A + 1, \phi_B)$. The application of \hat{B} without \hat{A} is equivalent to $(\theta, \phi_A, \phi_B) \rightarrow (\theta, \phi_A, \phi_B + 1)$. The simultaneous application of \hat{A} and \hat{B} is equivalent to the transformation $(\theta, \phi_A, \phi_B) \rightarrow (\theta, \phi_A + 1, \phi_B + 1)$. Note that we never act on the network itself (θ is never changed).

1. ZZ-operations

Let $|\psi_\theta\rangle$ be an arbitrary ansatz for the state of a system of N spin-1/2 particles, and

$$\hat{A} = \exp\{\alpha \hat{\sigma}_\mu^z \hat{\sigma}_\nu^z\} = \sum_x e^{\alpha x_\mu x_\nu} |x\rangle\langle x| \equiv \sum_x A_x |x\rangle\langle x| \quad \text{with} \quad \mu, \nu \in [1, \dots, N]. \quad (\text{G5})$$

the ZZ-operation acting on spins μ and ν . To encode the action of \hat{A} as a change of parameters we define the improved ansatz

$$\psi_{\theta,\phi}(x) = (A_x)^\phi \psi_\theta(x) = e^{\alpha \phi x_\mu x_\nu} \psi_\theta(x) \equiv e^{\phi x_\mu x_\nu} \psi_\theta(x), \quad (\text{G6})$$

where, in the last equality, we absorb α in the parameter ϕ without loss of generality. As expected, $|\psi_{\theta,\phi}\rangle \rightarrow \hat{A}|\psi_{\theta,\phi}\rangle \equiv (\theta, \phi) \rightarrow (\theta, \phi + 1)$. This ansatz accounts for the application of ZZ-operations on a fixed pair of spins, namely spin μ and ν . For this reason the additional parameter ϕ is a scalar. In general, however, we want to reserve the right to apply the operation between any pair of spins and/or on multiple pairs simultaneously.

Lets consider then the application of ZZ-rotations of two pairs of spins: (μ, ν) and (μ', ν') . In other words, we want to find an ansatz to incorporate the action of $\hat{A} = \exp\{\alpha_{\mu\nu} \hat{\sigma}_\mu^z \hat{\sigma}_\nu^z\}$, of $\hat{B} = \exp\{\alpha_{\mu'\nu'} \hat{\sigma}_{\mu'}^z \hat{\sigma}_{\nu'}^z\}$, and of their product AB , as a simple change of parameters [115]. To do so we can incorporate the single-operator ansatz from Eq. (G6) into the two-operator structure in Eq. (G4) as

$$\psi_{\theta,\phi}(x) = (B_x)^{\phi_{\mu'\nu'}} (A_x)^{\phi_{\mu\nu}} \psi_\theta(x) = \exp\{x_\mu \phi_{\mu\nu} x_\nu\} \exp\{x_{\mu'} \phi_{\mu'\nu'} x_{\nu'}\} \psi_\theta(x) = \exp\{x_\mu \phi_{\mu\nu} x_\nu + x_{\mu'} \phi_{\mu'\nu'} x_{\nu'}\} \psi_\theta(x). \quad (\text{G7})$$

Note that now $\phi = (\phi_{\mu\nu}, \phi_{\mu'\nu'})$ is a two-dimensional vector. This can be further generalized to account for ZZ-operations between any two spins via the ansatz

$$\psi_{\theta,\phi}(x) = \exp\left\{\sum_{ij} x_i \phi_{ij} x_j\right\} \psi_\theta(x) = \exp\{\mathbf{x} \boldsymbol{\phi} \mathbf{x}^T\} \psi_\theta(x). \quad (\text{G8})$$

Note that the multiplicative layer added to the network is exactly a two-body Jastrow ansatz where $\phi = [\phi_{\mu\nu}]$ is an $N \times N$ matrix. Application of the operator $\hat{A}_{\mu\nu} = \exp\{\alpha_{\mu\nu} \hat{\sigma}_\mu^z \hat{\sigma}_\nu^z\}$ is equivalent to the parameter transformation $\phi_{\mu\nu} \rightarrow \phi_{\mu\nu} + \alpha_{\mu\nu}$. In general we parameterize the log-amplitude of the wave function $\log \psi_{\theta,\phi}(x) = \mathbf{x} \boldsymbol{\phi} \mathbf{x}^T + \log \psi_\theta(x)$, so that the multiplicative layer actually becomes an additive one.

Appendix H: Neural network architectures

In this section we review the two architectures used in this work.

1. Convolutional neural networks

Convolutional Neural Networks (CNNs) are particularly well-suited for processing and analyzing grid-like data, such as images or quantum systems on a lattice. The architecture of a CNN consists of multiple layers indexed by $\ell \in [1, N_L]$, typically structured as alternating non-linear and affine transformations. For a system defined on a square lattice of linear length L and number of particles $N = L^2$, the input layer ($\ell = 1$) receives the configuration vector $x = (s_1, \dots, s_N)$, which is reshaped into an $L \times L$ matrix as $X = \text{vec}^{-1}(x)$, where vec represents the vectorization operation [116].

The building block of CNNs is the convolutional layer, where filters (or kernels) are applied to local regions of the input, learning spatial hierarchies of features. This is analogous to performing convolution operations over a lattice, capturing local correlations across the system. Let the output of the ℓ -th layer be

$$X^{(\ell)} = [X^{(\ell)}]_{i,j}^\alpha \in \mathbb{C}^{C_\ell} \otimes \mathbb{C}^{H_\ell \times W_\ell} \quad \text{with} \quad \begin{cases} i \in [0, H_\ell - 1], \\ j \in [0, W_\ell - 1], \\ \alpha \in [0, C_\ell - 1] \end{cases} \quad (\text{H1})$$

where (H_ℓ, W_ℓ) are the height and width of the processed data at layer step ℓ , and C_ℓ is the number of channels. The convolution operation yielding the data structure of the $(\ell + 1)$ -th layer is

$$\left(X^{(\ell+1)}\right)_{m,n}^\beta = \sigma_\ell \left([X^{(\ell)} \otimes F^{(\ell)}]_{m,n}^\beta \right) = \sigma_\ell \left(\sum_\alpha \sum_{i,j} [F^{(\ell)}]_{i,j}^{\alpha\beta} [X^{(\ell)}]_{m+i, n+j}^\alpha \right) \quad \text{with} \quad \begin{cases} i \in [0, h_\ell - 1], \\ j \in [0, w_\ell - 1], \\ \beta \in [0, c_\ell - 1] \end{cases} \quad (\text{H2})$$

where σ_ℓ is the activation function, (h_ℓ, w_ℓ) is the size of the convolutional kernel $F^{(\ell)}$, and c_ℓ is its output dimension.

For the activation functions, we follow the approach in Ref. [49]. The activation function in the first layer is the first three non-vanishing terms of the series expansion of $\ln \cos \mathcal{L}(z)$, ensuring the incorporation of the system's \mathbb{Z}_2 symmetry in the absence of bias in the first layer. It is defined as

$$\sigma_1(z) = \frac{z^2}{2} - \frac{z^4}{12} + \frac{z^6}{45}. \quad (\text{H3})$$

In subsequent layers, its derivative is used

$$\sigma_{\ell>1}(z) = \frac{z}{2} - \frac{z^3}{3} + \frac{2}{15}z^5. \quad (\text{H4})$$

We use circular padding to respect periodic boundary conditions, ensuring moreover that the spatial dimensions remain constant across layers, $H_\ell = W_\ell = L$. Both dilation and stride are set to one across all layers, and a fixed kernel size $h_\ell = w_\ell = k$ is used.

The CNN structure is then parameterized by a tuple $\Theta_{\text{CNN}} = (c_1, \dots, c_{N_L}; k)$, where c_ℓ represents the number of channels in each layer, and k denotes the kernel size. After the convolutional layers, a fully connected layer integrates the learned features, providing a global representation of the state. A sketch of the architecture is shown in Fig. 11.

2. Vision Transformer

The Vision Transformer (ViT) is a state-of-the-art architecture in machine learning. While originally developed for image classification and segmentation, it was recently adapted to the quantum many-body framework by Ref. [39, 102]. Below, we describe the key components and parameters of this architecture as applied to NQS.

The input consists of a configuration vector $x = (s_1, \dots, s_N)$, where each $s_i \in \{\pm 1\}$ represents the configuration of spin i on the lattice. The configuration is reshaped into an $L \times L$ matrix $X = \text{vec}^{-1}(x)$, with vec representing the vectorization operation [116]. This matrix corresponds to the lattice configuration of spins. The different layers of the ViT are as follows.

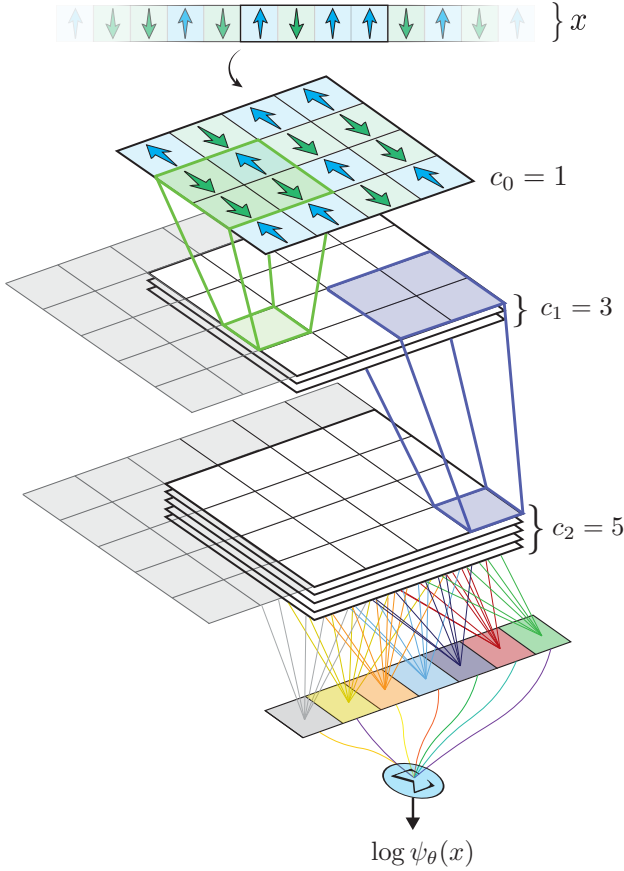


FIG. 11. Illustrative representation of the CNN architecture described in Appendix H1.

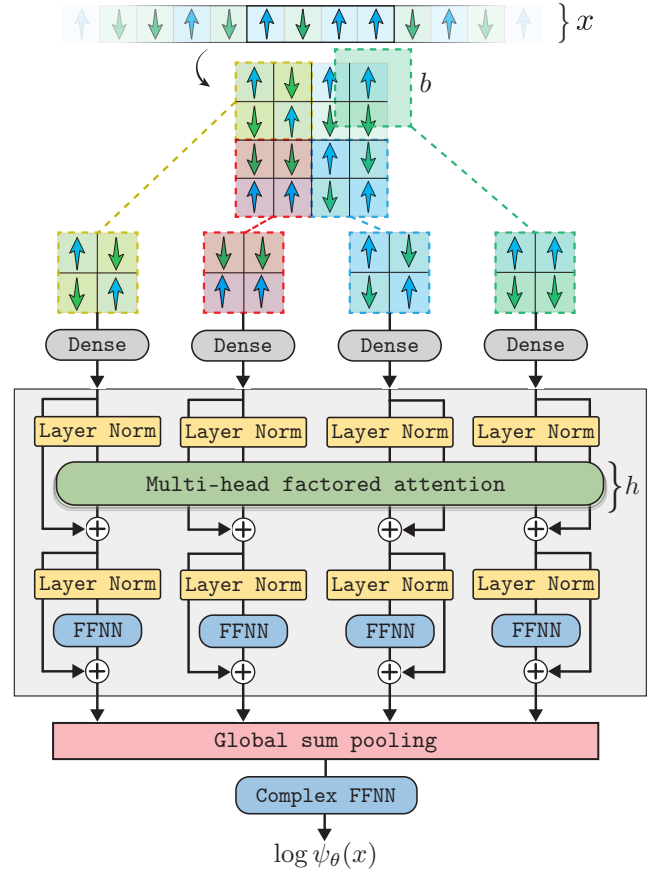


FIG. 12. Illustrative representation of the ViT architecture described in Appendix H2. We refer to Refs. [39, 102] for further details.

Patch Extraction and Embedding The matrix is divided into non-overlapping patches of size $b \times b$. Each patch is flattened, and linearly projected into a high-dimensional embedding space of dimension d . This transforms the spin values into a vector representation that is processed by the encoder blocks.

Encoder Blocks The core of the ViT architecture consists of N_L encoder blocks. Each encoder block processes the embedded patches independently, making it ideal for capturing long-range correlations and intricate interactions in the quantum system. The number of layers in this block is crucial for modeling complex quantum states. Each block consists of the following components:

Multi-Head Factored Attention Mechanism: Each encoder block includes a multi-head attention mechanism with h attention heads to capture the interactions between different patches. The attention weights are real-valued and translationally invariant, preserving the symmetry of the lattice which is only broken at the embedding stage only at the level of the patches. This mechanism allows the model to capture multiple aspects of the spin interactions across the system, with each attention head focusing on different representations of the patches. For a more detailed discussion of how this attention mechanism differs from the Multi-Head Self-Attention Mechanism typically used in machine learning applications, we refer the reader to Refs. [39, 102].

Feed-Forward Neural Network (FFN): A feed-forward neural network processes the output of the attention layer. The hidden layer in the FFN has a dimensionality of $n_{\text{up}}d$, where d is the embedding dimension, and n_{up} is an upscaling factor. A GeLU (Gaussian Error Linear Unit) activation function is used between the layers of the FFN, introducing non-linearity that help the model capture more complex features.

Skip Connections and Layer Normalization: Skip connections are applied across the attention and FFN layers. These connections help alleviate the vanishing gradient problem, allowing the model to train deeper architectures. Layer normalization is applied before both the attention and FFN layers to stabilize the training process and improve convergence.

Output and Wave Function Representation After the spin configuration passes through the encoder blocks, the output vectors corresponding to each patch are summed to create a final hidden representation vector z . This vector represents the configuration in a high-dimensional space and is passed through a final complex-valued fully connected neural network yielding the log-amplitude of our variational wave function.

We summarize the ViT configuration with the tuple $\Theta_{\text{ViT}} = (b, h, d/h, n_{\text{up}}; N_L)$. A schematic representation is shown in Fig. 12.

-
- [1] I. Georgescu, S. Ashhab and F. Nori, *Quantum simulation*, [Reviews of Modern Physics](#) **86**, 153–185 (2014).
 - [2] J. Preskill, *Quantum Computing in the NISQ era and beyond*, [Quantum](#) **2**, 79 (2018).
 - [3] O. Ezratty, *Understanding Quantum Technologies 2023*, (2021), [10.48550/ARXIV.2111.15352](#).
 - [4] X. Yuan, S. Endo, Q. Zhao, Y. Li and S. C. Benjamin, *Theory of variational quantum simulation*, [Quantum](#) **3**, 191 (2019).
 - [5] M. C. Bañuls, *Tensor Network Algorithms: A Route Map*, [Annual Review of Condensed Matter Physics](#) **14**, 173–191 (2023).
 - [6] R. Orús, *Tensor networks for complex quantum systems*, [Nature Reviews Physics](#) **1**, 538 (2019).
 - [7] U. Schollwöck, *The density-matrix renormalization group*, [Reviews of Modern Physics](#) **77**, 259–315 (2005).
 - [8] N. Feldman, A. Kshetrimayum, J. Eisert and M. Goldstein, *Entanglement Estimation in Tensor Network States via Sampling*, [PRX Quantum](#) **3** (2022), [10.1103/prxquantum.3.030312](#).
 - [9] J. Eisert, *Entanglement and tensor network states*, [Modeling and Simulation](#) **3**, 520 (2013) (2013), [arXiv:1308.3318](#).
 - [10] A. H. Werner, D. Jaschke, P. Silvi, M. Kliesch, T. Calarco, J. Eisert and S. Montangero, *Positive Tensor Network Approach for Simulating Open Quantum Many-Body Systems*, [Phys. Rev. Lett.](#) **116**, 237201 (2016).
 - [11] J. I. Cirac, D. Pérez-García, N. Schuch and F. Verstraete, *Matrix product states and projected entangled pair states: Concepts, symmetries, theorems*, [Reviews of Modern Physics](#) **93** (2021), [10.1103/revmodphys.93.045003](#).
 - [12] S. Paeckel, T. Köhler, A. Swoboda, S. R. Manmana, U. Schollwöck and C. Hubig, *Time-evolution methods for matrix-product states*, [Annals of Physics](#) **411**, 167998 (2019).
 - [13] S. Paeckel, T. Köhler, A. Swoboda, S. R. Manmana, U. Schollwöck and C. Hubig, *Time-evolution methods for matrix-product states*, [Annals of Physics](#) **411**, 167998 (2019).
 - [14] R. Orús, *A practical introduction to tensor networks: Matrix product states and projected entangled pair states*, [Annals of Physics](#) **349**, 117–158 (2014).
 - [15] U. Schollwöck, *The density-matrix renormalization group in the age of matrix product states*, [Annals of Physics](#) **326**, 96–192 (2011).
 - [16] M. Lubasch, J. I. Cirac and M.-C. Bañuls, *Unifying projected entangled pair state contractions*, [New Journal of Physics](#) **16**, 033014 (2014).
 - [17] F. Verstraete and J. I. Cirac, *Renormalization algorithms for Quantum-Many Body Systems in two and higher dimensions*, (2004), [10.48550/ARXIV.COND-MAT/0407066](#).
 - [18] L. Tagliacozzo, G. Evenbly and G. Vidal, *Simulation of two-dimensional quantum systems using a tree tensor network that exploits the entropic area law*, [Phys. Rev. B](#) **80**, 235127 (2009).
 - [19] T. Felser, S. Notarnicola and S. Montangero, *Efficient Tensor Network Ansatz for High-Dimensional Quantum Many-Body Problems*, [Physical Review Letters](#) **126** (2021), [10.1103/physrevlett.126.170603](#).
 - [20] P. Silvi, F. Tschirsich, M. Gerster, J. Jünemann, D. Jaschke, M. Rizzi and S. Montangero, *The Tensor Networks Anthology: Simulation techniques for many-body quantum lattice systems*, [SciPost Physics Lecture Notes](#) (2019), [10.21468/scipostphyslectnotes.8](#).
 - [21] D. Jaschke, S. Montangero and L. D. Carr, *One-dimensional many-body entangled open quantum systems with tensor network methods*, [Quantum Science and Technology](#) **4**, 013001 (2018).
 - [22] D. Jaschke, M. L. Wall and L. D. Carr, *Open source Matrix Product States: Opening ways to simulate entangled many-body quantum systems in one dimension*, [Computer Physics Communications](#) **225**, 59–91 (2018).
 - [23] G. Evenbly and G. Vidal, *Tensor Network States and Geometry*, [Journal of Statistical Physics](#) **145**, 891–918 (2011).
 - [24] G. Carleo and M. Troyer, *Solving the quantum many-body problem with artificial neural networks*, [Science](#) **355**, 602–606 (2017).
 - [25] O. Sharir, A. Shashua and G. Carleo, *Neural tensor contractions and the expressive power of deep neural quantum states*, [Phys. Rev. B](#) **106**, 205136 (2022).
 - [26] D.-L. Deng, X. Li and S. Das Sarma, *Quantum Entanglement in Neural Network States*, [Phys. Rev. X](#) **7**, 021021 (2017).
 - [27] J. Ureña, A. Sojo, J. Bermejo-Vega and D. Manzano, *Entanglement detection with classical deep neural networks*, [Scientific Reports](#) **14** (2024), [10.1038/s41598-024-68213-0](#).
 - [28] G. Passetti and D. M. Kennes, *Entanglement transition in deep neural quantum states*, (2023), [10.48550/ARXIV.2312.11941](#).
 - [29] G. Torlai and R. G. Melko, *Latent Space Purification via Neural Density Operators*, [Physical Review Letters](#) **120** (2018), [10.1103/physrevlett.120.240503](#).
 - [30] F. Vicentini, R. Rossi and G. Carleo, *Positive-definite parametrization of mixed quantum states with deep neural networks* (2022).
 - [31] D. Luo, Z. Chen, J. Carrasquilla and B. K. Clark, *Autoregressive Neural Network for Simulating Open Quantum Systems*

- via a Probabilistic Formulation, *Physical Review Letters* **128** (2022), [10.1103/physrevlett.128.090501](https://doi.org/10.1103/physrevlett.128.090501).
- [32] F. Vicentini, A. Biella, N. Regnault and C. Ciuti, *Variational Neural-Network Ansatz for Steady States in Open Quantum Systems*, *Physical Review Letters* **122** (2019), [10.1103/physrevlett.122.250503](https://doi.org/10.1103/physrevlett.122.250503).
- [33] D. Eeltink, F. Vicentini and V. Savona, *Variational dynamics of open quantum systems in phase space* (2023).
- [34] S. Dash, L. Gravina, F. Vicentini, M. Ferrero and A. Georges, *Efficiency of neural quantum states in light of the quantum geometric tensor*, (2024), [10.48550/ARXIV.2402.01565](https://arxiv.org/abs/2402.01565).
- [35] H. Zhao, G. Carleo and F. Vicentini, *Empirical Sample Complexity of Neural Network Mixed State Reconstruction*, *Quantum* **8**, 1358 (2024).
- [36] K. Choo, T. Neupert and G. Carleo, *Two-dimensional frustrated J_1 – J_2 model studied with neural network quantum states*, *Phys. Rev. B* **100**, 125124 (2019).
- [37] O. Sharir, Y. Levine, N. Wies, G. Carleo and A. Shashua, *Deep Autoregressive Models for the Efficient Variational Simulation of Many-Body Quantum Systems*, *Phys. Rev. Lett.* **124**, 020503 (2020).
- [38] D. Wu, R. Rossi, F. Vicentini, N. Astrakhantsev, F. Becca, X. Cao, J. Carrasquilla, F. Ferrari, A. Georges, M. Hibat-Allah, M. Imada, A. M. Läuchli, G. Mazzola, A. Mezzacapo, A. Millis, J. R. Moreno, T. Neupert, Y. Nomura, J. Nys, O. Parcollet, R. Pohle, I. Romero, M. Schmid, J. M. Silvester, S. Sorella, L. F. Tocchio, L. Wang, S. R. White, A. Wietek, Q. Yang, Y. Yang, S. Zhang and G. Carleo, *Variational Benchmarks for Quantum Many-Body Problems*, (2023), [10.48550/ARXIV.2302.04919](https://arxiv.org/abs/2302.04919).
- [39] L. L. Viteritti, R. Rende and F. Becca, *Transformer Variational Wave Functions for Frustrated Quantum Spin Systems*, *Phys. Rev. Lett.* **130**, 236401 (2023).
- [40] X. Liang, W.-Y. Liu, P.-Z. Lin, G.-C. Guo, Y.-S. Zhang and L. He, *Solving frustrated quantum many-particle models with convolutional neural networks*, *Phys. Rev. B* **98**, 104426 (2018).
- [41] J. Stokes, J. R. Moreno, E. A. Pnevmatikakis and G. Carleo, *Phases of two-dimensional spinless lattice fermions with first-quantized deep neural-network quantum states*, *Phys. Rev. B* **102**, 205122 (2020).
- [42] A. Szabó and C. Castelnovo, *Neural network wave functions and the sign problem*, *Phys. Rev. Res.* **2**, 033075 (2020).
- [43] K. Choo, A. Mezzacapo and G. Carleo, *Fermionic neural-network states for ab-initio electronic structure*, *Nature Communications* **11** (2020), [10.1038/s41467-020-15724-9](https://doi.org/10.1038/s41467-020-15724-9).
- [44] G. Cassella, H. Sutterud, S. Azadi, N. D. Drummond, D. Pfau, J. S. Spencer and W. M. C. Foulkes, *Discovering Quantum Phase Transitions with Fermionic Neural Networks*, *Phys. Rev. Lett.* **130**, 036401 (2023).
- [45] J. Robledo Moreno, G. Carleo, A. Georges and J. Stokes, *Fermionic wave functions from neural-network constrained hidden states*, *Proceedings of the National Academy of Sciences* **119** (2022), [10.1073/pnas.2122059119](https://doi.org/10.1073/pnas.2122059119).
- [46] G. Carleo, L. Cevolani, L. Sanchez-Palencia and M. Holzmann, *Unitary Dynamics of Strongly Interacting Bose Gases with the Time-Dependent Variational Monte Carlo Method in Continuous Space*, *Physical Review X* **7** (2017), [10.1103/physrevx.7.031026](https://doi.org/10.1103/physrevx.7.031026).
- [47] A. Sinibaldi, C. Giuliani, G. Carleo and F. Vicentini, *Unbiasing time-dependent Variational Monte Carlo by projected quantum evolution*, *Quantum* **7**, 1131 (2023).
- [48] J. Stokes, B. Chen and S. Veerapaneni, *Numerical and geometrical aspects of flow-based variational quantum Monte Carlo*, *Machine Learning: Science and Technology* **4**, 021001 (2023).
- [49] M. Schmitt and M. Heyl, *Quantum Many-Body Dynamics in Two Dimensions with Artificial Neural Networks*, *Physical Review Letters* **125** (2020), [10.1103/physrevlett.125.100503](https://doi.org/10.1103/physrevlett.125.100503).
- [50] T. Mendes-Santos, M. Schmitt and M. Heyl, *Highly Resolved Spectral Functions of Two-Dimensional Systems with Neural Quantum States*, *Phys. Rev. Lett.* **131**, 046501 (2023).
- [51] A. Joshi, R. Peters and T. Posske, *Quantum skyrmion dynamics studied by neural network quantum states*, *Physical Review B* **110** (2024), [10.1103/physrevb.110.104411](https://doi.org/10.1103/physrevb.110.104411).
- [52] L. Mauron, Z. Denis, J. Nys and G. Carleo, *Predicting Topological Entanglement Entropy in a Rydberg analog simulator* (2024).
- [53] J. Nys, G. Pescia, A. Sinibaldi and G. Carleo, *Ab-initio variational wave functions for the time-dependent many-electron Schrödinger equation* (2024).
- [54] D. Wagner, A. Klümper and J. Sirker, *Thermodynamics based on neural networks*, *Physical Review B* **109** (2024), [10.1103/physrevb.109.155128](https://doi.org/10.1103/physrevb.109.155128).
- [55] J. Nys, Z. Denis and G. Carleo, *Real-time quantum dynamics of thermal states with neural thermofields*, *Phys. Rev. B* **109**, 235120 (2024).
- [56] F. Vicentini, R. Rossi and G. Carleo, *Positive-definite parametrization of mixed quantum states with deep neural networks* (2022).
- [57] J. Lin, D. Luo, X. Yao and P. E. Shanahan, *Real-time dynamics of the Schwinger model as an open quantum system with Neural Density Operators*, *Journal of High Energy Physics* **2024** (2024), [10.1007/jhep06\(2024\)211](https://doi.org/10.1007/jhep06(2024)211).
- [58] L. F. Shampine and C. W. Gear, *A User's View of Solving Stiff Ordinary Differential Equations*, *SIAM Review* **21**, 1–17 (1979).
- [59] K. Donatella, Z. Denis, A. Le Boité and C. Ciuti, *Dynamics with autoregressive neural quantum states: Application to critical quench dynamics*, *Phys. Rev. A* **108**, 022210 (2023).
- [60] W. Zhang, B. Xing, X. Xu and D. Poletti, *Paths towards time evolution with larger neural-network quantum states*, (2024), [10.48550/ARXIV.2406.03381](https://arxiv.org/abs/2406.03381).
- [61] M. Medvidović and G. Carleo, *Classical variational simulation of the Quantum Approximate Optimization Algorithm*, *npj Quantum Information* **7** (2021), [10.1038/s41534-021-00440-z](https://doi.org/10.1038/s41534-021-00440-z).
- [62] B. Jónsson, B. Bauer and G. Carleo, *Neural-network states for the classical simulation of quantum computing* (2018).

- [63] I. L. Gutiérrez and C. B. Mendl, *Real time evolution with neural-network quantum states*, [Quantum](#) **6**, 627 (2022).
- [64] M. Medvidović and J. R. Moreno, *Neural-network quantum states for many-body physics*, [The European Physical Journal Plus](#) **139** (2024), [10.1140/epjp/s13360-024-05311-y](#).
- [65] H. Lange, A. Van de Walle, A. Abedinnia and A. Bohrdt, *From Architectures to Applications: A Review of Neural Quantum States*, (2024), [10.48550/ARXIV.2402.09402](#).
- [66] N. Hatano and M. Suzuki, *Finding Exponential Product Formulas of Higher Orders*, in [Quantum Annealing and Other Optimization Methods](#) (Springer Berlin Heidelberg, 2005) p. 37–68.
- [67] A. Müller-Hermes, J. Ignacio Cirac and M. C. Bañuls, *Tensor network techniques for the computation of dynamical observables in one-dimensional quantum spin systems*, [New Journal of Physics](#) **14**, 075003 (2012).
- [68] C. Moler and C. Van Loan, *Nineteen Dubious Ways to Compute the Exponential of a Matrix, Twenty-Five Years Later*, [SIAM Review](#) **45**, 3–49 (2003).
- [69] Acting diagonally in the computational basis means that $\langle a | \hat{Z} | b \rangle \propto \delta_{ab}$.
- [70] V. Havlicek, *Amplitude Ratios and Neural Network Quantum States*, [Quantum](#) **7**, 938 (2023).
- [71] E. Ledinauskas and E. Anisimovas, *Scalable imaginary time evolution with neural network quantum states*, [SciPost Physics](#) **15** (2023), [10.21468/scipostphys.15.6.229](#).
- [72] D. P. Kingma and J. Ba, *Adam: A Method for Stochastic Optimization*, (2014), [10.48550/ARXIV.1412.6980](#).
- [73] J. Martens and I. Sutskever, *Training Deep and Recurrent Networks with Hessian-Free Optimization*, in [Neural Networks: Tricks of the Trade](#) (Springer Berlin Heidelberg, 2012) p. 479–535.
- [74] J. Martens, *New Insights and Perspectives on the Natural Gradient Method*, [Journal of Machine Learning Research](#) **21**, 1 (2020).
- [75] J. Nocedal and S. J. Wright, [Numerical Optimization](#), Springer Series in Operations Research and Financial Engineering, Vol. 2 (Springer New York, 2006).
- [76] R. Cheng, *Quantum Geometric Tensor (Fubini-Study Metric) in Simple Quantum System: A pedagogical Introduction* (2010).
- [77] J. Stokes, J. Izaac, N. Killoran and G. Carleo, *Quantum Natural Gradient*, [Quantum](#) **4**, 269 (2020).
- [78] The expression of the QGT given in Eq. (13) holds for a generic variational state $|\psi\rangle$. It is used to compute the natural gradient as $\mathbf{S}^{-1} \nabla \mathcal{L}(|\psi\rangle, |\phi\rangle)$. In p-tVMC the variational state is often transformed by the operator \hat{V} and we are interested in computing the natural gradient associated to $\nabla \mathcal{L}(|\tilde{\psi}\rangle, |\phi\rangle)$, with $|\tilde{\psi}\rangle = \hat{V} |\psi\rangle$ and $|\phi\rangle$ an arbitrary target state. This is again given by Eq. (13) following the replacement $\psi \rightarrow \tilde{\psi}$. In ?? we provide an efficient way of computing this quantity without having to sample from the transformed state.
- [79] We note that the identity $\nabla \mathcal{L} = \mathbf{X} \varepsilon$ does not hold universally for all loss functions, although it is verified for many prototypical choices, such as the mean squared error or the variational energy. In Section III, we demonstrate that the fidelity can exhibit this structure, although this is not guaranteed for all estimators of its gradient.
- [80] T. Heskes, *On “Natural” Learning and Pruning in Multilayered Perceptrons*, [Neural Computation](#) **12**, 881–901 (2000).
- [81] R. Grosse and R. Salakhudinov, in [Proceedings of the 32nd International Conference on Machine Learning](#), Proceedings of Machine Learning Research, Vol. 37, edited by F. Bach and D. Blei (PMLR, Lille, France, 2015) pp. 2304–2313.
- [82] J. Martens and R. Grosse, in [Proceedings of the 32nd International Conference on Machine Learning](#), Proceedings of Machine Learning Research, Vol. 37, edited by F. Bach and D. Blei (PMLR, Lille, France, 2015) pp. 2408–2417.
- [83] R. Grosse and J. Martens, in [Proceedings of The 33rd International Conference on Machine Learning](#), Proceedings of Machine Learning Research, Vol. 48, edited by M. F. Balcan and K. Q. Weinberger (PMLR, New York, New York, USA, 2016) pp. 573–582.
- [84] Y. Ollivier, *Riemannian metrics for neural networks I: feedforward networks*, [Information and Inference](#) **4**, 108–153 (2015).
- [85] S.-i. Amari, R. Karakida and M. Oizumi, in [Proceedings of the Twenty-Second International Conference on Artificial Intelligence and Statistics](#), Proceedings of Machine Learning Research, Vol. 89, edited by K. Chaudhuri and M. Sugiyama (PMLR, 2019) pp. 694–702.
- [86] R. Karakida and K. Osawa, *Understanding approximate Fisher information for fast convergence of natural gradient descent in wide neural networks**, [Journal of Statistical Mechanics: Theory and Experiment](#) **2021**, 124010 (2021).
- [87] Q. Bai, S. Rosenberg and W. Xu, *A Geometric Understanding of Natural Gradient* (2022).
- [88] A. Chen and M. Heyl, *Empowering deep neural quantum states through efficient optimization*, [Nature Physics](#) **20**, 1476–1481 (2024).
- [89] K. B. Petersen and M. S. Pedersen, [The Matrix Cookbook](#) (2012).
- [90] R. Rende, L. L. Viteritti, L. Bardone, F. Becca and S. Goldt, *A simple linear algebra identity to optimize large-scale neural network quantum states*, [Communications Physics](#) **7** (2024), [10.1038/s42005-024-01732-4](#).
- [91] A. Jacot, F. Gabriel and C. Hongler (Curran Associates Inc., Red Hook, NY, USA, 2018) p. 8580–8589.
- [92] R. Novak, J. Sohl-Dickstein and S. S. Schoenholz, in [Proceedings of the 39th International Conference on Machine Learning](#), Proceedings of Machine Learning Research, Vol. 162, edited by K. Chaudhuri, S. Jegelka, L. Song, C. Szepesvari, G. Niu and S. Sabato (PMLR, 2022) pp. 17018–17044.
- [93] As $|\psi\rangle \rightarrow |\phi\rangle$, the optimal choice for c has been shown to converge to $c = -1/2$.
- [94] R. Y. Rubinstein and D. P. Kroese, [Simulation and the Monte Carlo Method](#) (Wiley, 2016) Chap. 5.
- [95] R. Ranganath, S. Gerrish and D. Blei, in [Artificial intelligence and statistics](#) (PMLR, 2014) pp. 814–822.
- [96] Contrary to standard observables, the projector \hat{H} is dense (or not K-local), therefore its local estimator $H_{\text{loc}}(x)$ cannot be computed exactly and is instead estimated itself.
- [97] J. Gacon, J. Nys, R. Rossi, S. Woerner and G. Carleo, *Variational quantum time evolution without the quantum geometric*

- tensor, *Phys. Rev. Res.* **6**, 013143 (2024).
- [98] J. Martens et al., in *Icml*, Vol. 27 (2010) pp. 735–742.
- [99] In a trust-region approach to second-order optimization problems, an increase in λ_k corresponds to tightening the trust region. Conversely, a reduction in λ_k corresponds to a relaxation of the trust region [75].
- [100] G. Wanner and E. Hairer, *Solving ordinary differential equations II*, Vol. 375 (Springer Berlin Heidelberg New York, 1996).
- [101] P. Czarnik, J. Dziarmaga and P. Corboz, *Time evolution of an infinite projected entangled pair state: An efficient algorithm*, *Phys. Rev. B* **99**, 035115 (2019).
- [102] L. L. Viteritti, R. Rende, A. Parola, S. Goldt and F. Becca, *Transformer Wave Function for the Shastry-Sutherland Model: emergence of a Spin-Liquid Phase*, (2023), [10.48550/ARXIV.2311.16889](https://arxiv.org/abs/10.48550/ARXIV.2311.16889).
- [103] F. Vicentini, D. Hofmann, A. Szabó, D. Wu, C. Roth, C. Giuliani, G. Pescia, J. Nys, V. Vargas-Calderón, N. Astrakhantsev and G. Carleo, *NetKet 3: Machine Learning Toolbox for Many-Body Quantum Systems*, *SciPost Phys. Codebases*, **7** (2022).
- [104] G. Carleo, K. Choo, D. Hofmann, J. E. T. Smith, T. Westerhout, F. Alet, E. J. Davis, S. Efthymiou, I. Glasser, S.-H. Lin, M. Mauri, G. Mazzola, C. B. Mendl, E. van Nieuwenburg, O. O’Reilly, H. Thévéniaut, G. Torlai, F. Vicentini and A. Wietek, *NetKet: A Machine Learning Toolkit for Many-Body Quantum Systems*, *SoftwareX*, **100311** (2019).
- [105] D. Häfner and F. Vicentini, *mpi4jax: Zero-copy MPI communication of JAX arrays*, *Journal of Open Source Software* **6**, 3419 (2021).
- [106] J. Bradbury, R. Frostig, P. Hawkins, M. J. Johnson, C. Leary, D. Maclaurin, G. Necula, A. Paszke, J. VanderPlas, S. Wanderman-Milne and Q. Zhang, *JAX: composable transformations of Python+NumPy programs* (2018).
- [107] P. Kidger and C. Garcia, *Equinox: neural networks in JAX via callable PyTrees and filtered transformations*, Differentiable Programming workshop at Neural Information Processing Systems 2021 (2021).
- [108] J. Heek, A. Levskaya, A. Oliver, M. Ritter, B. Rondepierre, A. Steiner and M. van Zee, *Flax: A neural network library and ecosystem for JAX* (2024).
- [109] J. Johansson, P. Nation and F. Nori, *QuTiP: An open-source Python framework for the dynamics of open quantum systems*, *Computer Physics Communications* **183**, 1760 (2012).
- [110] J. Johansson, P. Nation and F. Nori, *QuTiP 2: A Python framework for the dynamics of open quantum systems*, *Computer Physics Communications* **184**, 1234 (2013).
- [111] R. P. Stanley, *Enumerative Combinatorics, Volume 2*, Cambridge Studies in Advanced Mathematics, Vol. 2 (Cambridge University Press, 1999).
- [112] U. M. Ascher, S. J. Ruuth and B. T. R. Wetton, *Implicit-Explicit Methods for Time-Dependent Partial Differential Equations*, *SIAM Journal on Numerical Analysis* **32**, 797–823 (1995).
- [113] U. M. Ascher, S. J. Ruuth and R. J. Spiteri, *Implicit-explicit Runge-Kutta methods for time-dependent partial differential equations*, *Applied Numerical Mathematics* **25**, 151–167 (1997).
- [114] R. Li, H. Ye, D. Jiang, X. Wen, C. Wang, Z. Li, X. Li, D. He, J. Chen, W. Ren and L. Wang, *A computational framework for neural network-based variational Monte Carlo with Forward Laplacian*, *Nature Machine Intelligence* (2024), [10.1038/s42256-024-00794-x](https://doi.org/10.1038/s42256-024-00794-x).
- [115] Here $\alpha_{\mu\nu} \in \mathbb{C}$ is the phase of the gate operation acting on the pair (μ, ν) .
- [116] F. Minganti, A. Miranowicz, R. W. Chhajlany and F. Nori, *Quantum exceptional points of non-Hermitian Hamiltonians and Liouvillians: The effects of quantum jumps*, *Physical Review A* **100** (2019), [10.1103/physreva.100.062131](https://doi.org/10.1103/physreva.100.062131).